Supplementary Information for

Towards complete linearly-polarized electroluminescence using isotropic emitters

Yangzhi Tan *et al.*

Corresponding authors.
Email:
wangk@sustech.edu.cn,
feng.gao@liu.se,
sunxw@sustech.edu.cn,
hwchoi@hku.hk

Table of Contents

Note S1. The intrinsic trade-off between polarization ratio (PR) and light extraction efficiency (LEE) in LP-LEDs based on manipulating the dipole orientation of anisotropic emitters

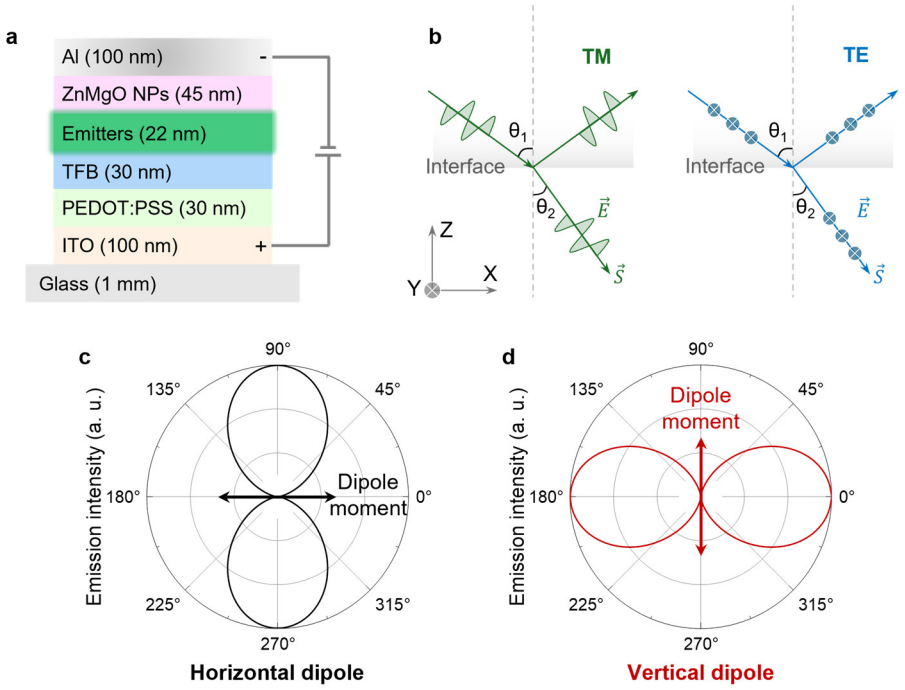

e

	Horizontal dipole	Vertical dipole
Direction of dipole moment *P*	*P* // X-Y plane (interface)	*P* ⊥ X-Y plane (interface)
Main emission direction *S*	*S* ⊥ X-Y plane (interface)	*S* // X-Y plane (interface)
Fractions of vertically-oriented transition dipole moment Θ_V	$\Theta_V = 0$	$\Theta_V = 1$

Figure S1. Principles of TDM orientation and polarization in a typical bottom-emitting LED structure that is widely used for QLEDs, NR-LEDs and NPL-LEDs. (a) Schematic architecture of a typical solution-processed bottom-emitting LED used as a model system. (b) Illustration of transverse magnetic (TM) and transverse electric (TE) polarized light interacting with a planar interface. ***E*** and ***S*** represent the electric field and Poynting vectors, respectively. (c, d) Simulated radiation patterns for a (c) horizontal dipole and (d) vertical dipole, illustrating their distinct emission profiles. (e) A table summarizing the key properties of horizontal and vertical dipoles and their corresponding fraction of vertically-oriented transition dipole moments (Θ_V).

The prevailing strategy for creating solution-processed LP-LEDs involves controlling the dipole orientation of anisotropic emitters, such as nanorods[1-3] (NRs) and nanoplatelets[4] (NPLs). However, this material-centric approach encounters a fundamental severe trade-off between achieving a high PR and a high LEE. Here, we elucidate the physical origins of this trade-off by analyzing a typical solution-processed bottom-emitting LED architecture which is widely used for high-performance quantum-dot (QD) LEDs (QLEDs)[5], NR-LEDs[6] and NPL-LEDs[7] (Fig. S1a), which serves as a representative model system.

The interaction of light with the planar interfaces within an LED stack is polarization-dependent. Emitted light can be decomposed into transverse magnetic (TM) and transverse electric (TE) modes (Fig. S1b). The electric field oscillation directions of both TM and TE modes are perpendicular to the direction of energy propagation (Poynting vector). The crucial distinction is that the electric field of the TM mode oscillates within the plane of incidence (XZ plane), while the TE mode's electric field oscillates perpendicular to it. For light propagating normal to the interfaces ($\theta = 0$), the electric fields of both modes are parallel to the interfaces. In this case, the modes are indistinguishable to the layered structure, and their optical response are identical. Conversely, for light at large propagation angles (grazing incidence, $\theta \rightarrow 90°$), the TM electric field has a significant component perpendicular to the interfaces while the TE field remains parallel. This geometric difference leads to a maximal divergence in their optical response, which is the foundational requirement for polarization splitting.

This polarization-dependent optical response must be considered in conjunction with the radiation patterns of the emitters themselves. The orientation of an emitter's transition dipole moment (TDM) dictates its emission pattern. This can be understood by considering two limiting cases: purely horizontal dipoles (TDM parallel to the device plane/interface, Fig. S1c) and purely vertical dipoles (TDM perpendicular to the device plane/interface, Fig. S1d). The fraction of vertically-oriented TDMs in an ensemble, Θ_V, quantifies this orientation, where $\Theta_V = 0$ for a perfectly horizontal alignment and $\Theta_V = 1$ for a perfectly vertical alignment (Fig. S1e). It is important to note that for typical isotropic emitters, such as near-spherical QDs, the TDM orientation is random. In a Cartesian coordinate system, the dipole moments are equally distributed along the X, Y, and Z axes, resulting in an ensemble average of $\Theta_V = 1/3$.

Synthesizing these concepts reveals an intrinsic dilemma. A high PR requires maximal differentiation between TE and TM modes, which only occurs at large emission angles ($\theta \rightarrow 90°$). Such a radiation pattern is characteristic of vertically aligned dipoles ($\Theta_V \rightarrow 1$). However, light emitted at these high angles is highly susceptible to total internal reflection (TIR), causing it to be trapped in waveguide modes in substrate (marked in SG) and functional layers in LED (marked in WG), leading to a drastically reduced LEE. Conversely, achieving a high LEE requires suppressing these trapped modes by favoring vertical emission ($\theta \rightarrow 0$), the characteristic pattern of horizontally aligned dipoles ($\Theta_V \rightarrow 0$). At these near-normal angles, however, the TE and TM modes are optically equivalent, resulting in nearly unpolarized emission (PR $\approx$ 1). This analysis aligns perfectly with experimental reports on NR-LEDs and NPL-LEDs, where high-efficiency devices require horizontally-aligned NRs[6,8] or face-down NPLs[7,9] ($\Theta_V \rightarrow 0$, LEE > 30%) and high-PR devices require vertically-aligned NRs[1] or edge-up NPLs[4] ($\Theta_V \rightarrow 1$), but at the cost of low efficiency (LEE < 5%).

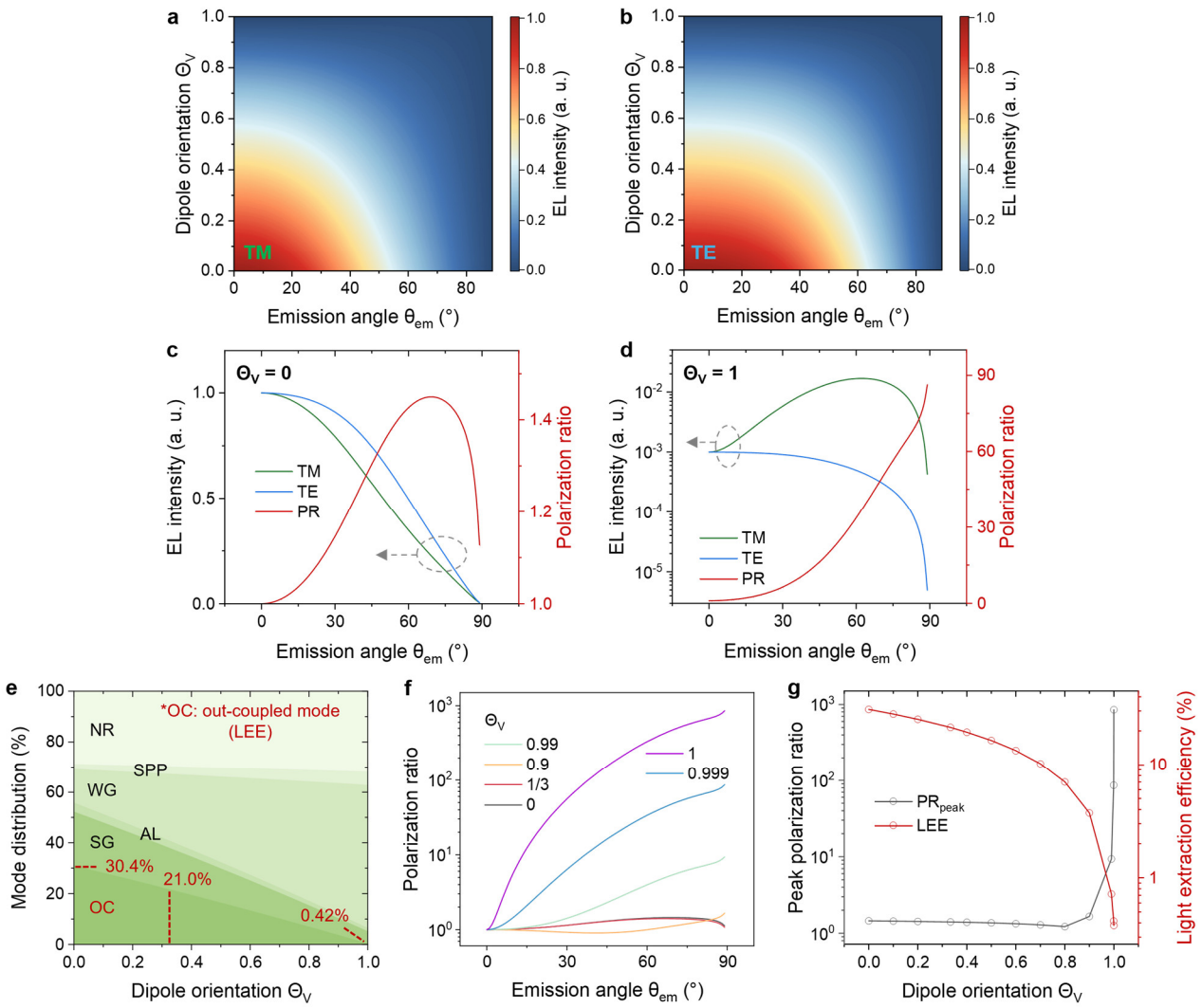

Figure S2. Simulated trade-off between LEE and PR in a typical bottom-emitting LED structure that is widely used for QLEDs, NR-LEDs and NPL-LEDs. (a, b) Simulated emission angle θ_{em}-resolved EL intensity as a function of dipole orientation Θ_V for (a) TM and (b) TE modes. (c, d) θ_{em}-dependent EL intensity and PR for two limiting cases: (c) a purely horizontal emitter system ($\Theta_V = 0$) and (d) a purely vertical emitter system ($\Theta_V = 1$). (e) Simulated power distribution into different optical channels as a function of Θ_V. The out-coupled (OC) mode fraction is equivalent to the LEE. (f) Simulated PR as a function of θ_{em} for various values of Θ_V. (g) The fundamental trade-off relationship between the calculated LEE and the peak achievable PR as a function of Θ_V.

To quantitatively validate this trade-off, we performed a comprehensive optical simulation using Setfos. The emission angle θ_{em}- and TDM orientation Θ_V- dependent EL intensity maps for both TM and TE modes (Figs. S2a, S2b) confirm our qualitative analysis. They show that for any given Θ_V, the EL intensity generally decreases with increasing emission angle θ_{em}. Besides, the overall EL intensity is strongest for horizontally-oriented emitters ($\Theta_V \rightarrow 0$) at near-normal angles ($\theta_{em} \rightarrow 0$) and reduces as the TDMs become more vertical ($\Theta_V \rightarrow 1$). The TM and TE intensities are comparable at near-normal angles ($\theta_{em} \rightarrow 0$) and only diverge significantly at grazing incidence. This behavior is clearly

illustrated by the two limiting cases. For a purely horizontal emitter system ($\Theta_V = 0$, Fig. S2c), the EL is intense and peaks at $\theta_{em} = 0$, but because the TM and TE intensities are similar, the PR remains below 1.5 across all angles. Conversely, for a purely vertical system ($\Theta_V = 1$, Fig. S2d), the overall emission is extremely weak, yet the PR increases dramatically with θ_{em} as the TM and TE intensities diverge, reaching a theoretical maximum of PR = 86 at $\theta_{em} = 90°$.

The mode distribution analysis (Fig. S2e) reveals the origin of this phenomenon: as Θ_V increases from 0 to 1, the fraction of power lost to WG mode rises, while the out-coupled (OC) mode fraction, which is equivalent to the LEE, decreases from a peak of 30.4% to a minimum of 0.42% (see Fig. S14 for a detailed description of all optical modes). Furthermore, achieving a high PR requires extreme vertical alignment ($\Theta_V \rightarrow 1$), with the PR remaining below 2 for all θ_{em} unless $\Theta_V > 0.9$ (Fig. S2f). For isotropic emitters with $\Theta_V = 1/3$ (red curve), the PR curve almost overlaps with that for $\Theta_V = 0$ (black curve). The direct, inverse relationship between LEE and peak PR is illustrated in Fig. S2g, which encapsulates this intrinsic dilemma. Our simulation results are consistent with previous experimental reports[1,4,6-9]: in a typical solution-processed LED architecture like that in Fig. S1a, a Θ_V close to 0 achieves high-efficiency EL with almost no linear-polarization characteristic, while a Θ_V close to 1 achieves a high PR only at the cost of drastically reduced efficiency. Achieving a PR above 10 in a typical solution-processed LED structure via TDM alignment would reduce the LEE to less than 0.8%, a severe loss compared to the 20–40% LEE of unpolarized LEDs[5,7]. This conclusion underscores the fundamental limitations of relying solely on TDM manipulation of anisotropic emitters.

Note S2. Methodology of back focal plane (BFP) imaging

The schematic of the optical system for BFP imaging was shown in Fig. S3a. A 405 nm diode laser was focused onto the printed QDs film using an oil-immersion objective (CFI Apo TIRF 60XC Oil). The sample was prepared on a cover slide with a thickness of 0.17 mm. The fluorescence emitted from the nanoplatelets was collected in the epi-fluorescence configuration through the same objective. The emitted signal was then directed through a dichroic mirror, passed through the 200 mm focal length tube lens of the inverted microscope (Nikon Ti-U), and further relayed via an additional 50 mm focal length lens. A polarizer was placed in the optical path before the fluorescence was finally captured by a monochrome CCD camera (Retiga R6).

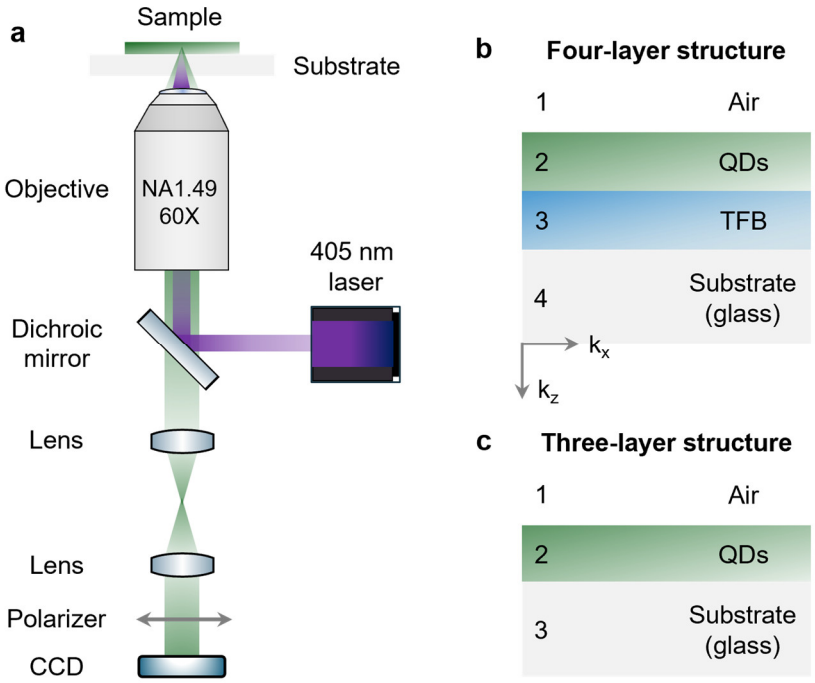

Figure S3. BFP imaging. (a) Schematic of the optical system for BFP imaging. (b) Four-layer and (c) three-layer structures involved in BFP imaging for the determination of Θ_V.

The BFP imaging simulations are based on previous works[10,11]. The optical intensity distribution in momentum space is calculated as:

$$\begin{cases} S^s(\omega,k_x) = C\tilde{\rho}^s_{IP}(\omega,k_x)\bar{n}_{IP}\left|\mu_{IP}\right|^2 \\ S^p(\omega,k_x) = C\left[\tilde{\rho}^p_{IP}(\omega,k_x)\bar{n}_{IP}\left|\mu_{IP}\right|^2 + \tilde{\rho}^p_{OP}(\omega,k_x)\bar{n}_{oP}\left|\mu_{oP}\right|^2\right] \end{cases} \quad (1)$$

where C is a constant determined by experiment conditions, $\bar{n}|\mu|^2$ is the Einstein coefficient for electric dipoles and the relative ratio of $\bar{n}_{IP}|\mu_{IP}|^2$ and $\bar{n}_{OP}|\mu_{OP}|^2$ determines the angle of the macroscopic dipole with the film's plane, and ρ is the density of electromagnetic modes.

The simulation of QDs on TFB is considered as a four-layer structure consisting of air, QDs, TFB layer and substrate (Fig. S3b), whereas QDs on substrate is considered as a three-layer structure consisting of air, QDs layer, and the substrate (Fig. S3c). The density of electromagnetic modes for four-layer and three-layer structure can be written as equations 2 and 3, respectively:

$$\begin{cases} \tilde{\rho}_{IP}^{s}\left(\omega,k_x\right)=C_2\left|\overline{t}_{32}^{s}e^{\frac{1}{2}ik_{2,z}^{s}D_{QD}}\overline{t}_{43}^{s}e^{ik_{3,z}^{s}D_{TFB}}\left(1+r_{21}^{s}e^{ik_{2,z}^{s}D_{QD}}\right)\right|^2 \\ \tilde{\rho}_{IP}^{p}\left(\omega,k_x\right)=C_2\left|\frac{k_{2,z}^{p}}{\sqrt{\epsilon_2^{p}}k_0}\overline{t}_{32}^{p}e^{\frac{1}{2}ik_{2,z}^{p}D_{QD}}\overline{t}_{43}^{p}e^{ik_{3,z}^{p}D_{TFB}}\left(1-r_{21}^{p}e^{ik_{2,z}^{p}D_{QD}}\right)\right|^2 \\ \tilde{\rho}_{OP}^{p}\left(\omega,k_x\right)=C_2\left|\frac{k_x}{\sqrt{\epsilon_2^{p}}k_0}\overline{t}_{32}^{p}e^{\frac{1}{2}ik_{2,z}^{p}D_{QD}}\overline{t}_{43}^{p}e^{ik_{3,z}^{p}D_{TFB}}\left(1+r_{21}^{p}e^{ik_{2,z}^{p}D_{QD}}\right)\right|^2 \end{cases} \tag{2}$$

$$\begin{cases} \tilde{\rho}_{IP}^{s}\left(\omega,k_x\right)=C_1\left|\overline{t}_{32}^{s}e^{\frac{1}{2}ik_{2,z}^{s}D_{QD}}\left(1+r_{21}^{s}e^{ikk_{2,z}^{s}D_{QD}}\right)\right|^2 \\ \tilde{\rho}_{IP}^{p}\left(\omega,k_x\right)=C_1\left|\frac{k_{2,z}^{p}}{\sqrt{\epsilon_2^{p}}k_0}\overline{t}_{32}^{p}e^{\frac{1}{2}ik_{2,z}^{p}D_{QD}}\left(1-r_{21}^{p}e^{ik_{2,z}^{p}D_{QD}}\right)\right|^2 \\ \tilde{\rho}_{OP}^{p}\left(\omega,k_x\right)=C_1\left|\frac{k_x}{\sqrt{\epsilon_2^{p}}k_0}\overline{t}_{32}^{p}e^{\frac{1}{2}ik_{2,z}^{p}D_{QD}}\left(1+r_{21}^{p}e^{ik_{2,z}^{p}D_{QD}}\right)\right|^2 \end{cases} \tag{3}$$

with the coefficient:

$$\begin{cases} C_1=\dfrac{1}{8\pi k_0^2}\dfrac{k_0}{k_{3,z}} \\ C_2=\dfrac{1}{8\pi k_0^2}\dfrac{k_0}{k_{4,z}} \end{cases} \tag{4}$$

where D_{QD} and D_{TFB} are the thickness of the QDs layer and TFB layer, respectively. Multiple reflections are taken into account by the Fabry-Pérot model defined as equations 5. The Fresnel coefficients are defined as equations 6. IP (in plane) dipole consists of x and y components. Since they have rotational symmetry, we need to only analyze the x component of the pattern.

Comparison of the experimental PL intensity profile (extracted along the dashed line in Fig. 1d) with simulation results is shown in Fig. 1e. Fitting yields a fraction of vertical transition dipole moments Θ_V of ~0.33, indicative of a macroscopic isotropic TDM distribution in the QDs film which is deposited onto TFB.

$$\begin{cases} \overline{t}_{32}^{s}=\dfrac{t_{32}^{s}}{1-r_{21}^{s}r_{23}^{s}e^{2ik_{2,z}^{s}D_{QD}}} \\ \overline{t}_{32}^{p}=\dfrac{t_{12}^{p}}{1-r_{21}^{p}r_{23}^{p}e^{2ik_{2,z}^{s}D_{QD}}} \\ \overline{t}_{43}^{s}=\dfrac{t_{32}^{s}}{1-r_{32}^{s}r_{34}^{s}e^{2ik_{3,z}^{s}D_{TFB}}} \\ \overline{t}_{43}^{p}=\dfrac{t_{12}^{p}}{1-r_{32}^{p}r_{34}^{p}e^{2ik_{3,z}^{s}D_{TFB}}} \end{cases} \tag{5}$$

$$\begin{cases} r_{ij}^{s}=\dfrac{k_{i,z}-k_{j,z}}{k_{i,z}+k_{j,z}} \\ t_{ij}^{s}=\dfrac{2k_{i,z}}{k_{i,z}+k_{j,z}} \\ r_{ij}^{p}=\dfrac{k_{i,z}\epsilon_j-k_{j,z}\epsilon_i}{k_{i,z}\epsilon_j+k_{j,z}\epsilon_i} \\ t_{ij}^{p}=\dfrac{2\sqrt{\epsilon_j}\sqrt{\epsilon_i}k_{i,z}}{k_{i,z}\epsilon_j+k_{j,z}\epsilon_i} \end{cases} \tag{6}$$

Note S3. Comparative analysis: CIPS LP-LED platform vs. traditional TDM manipulation

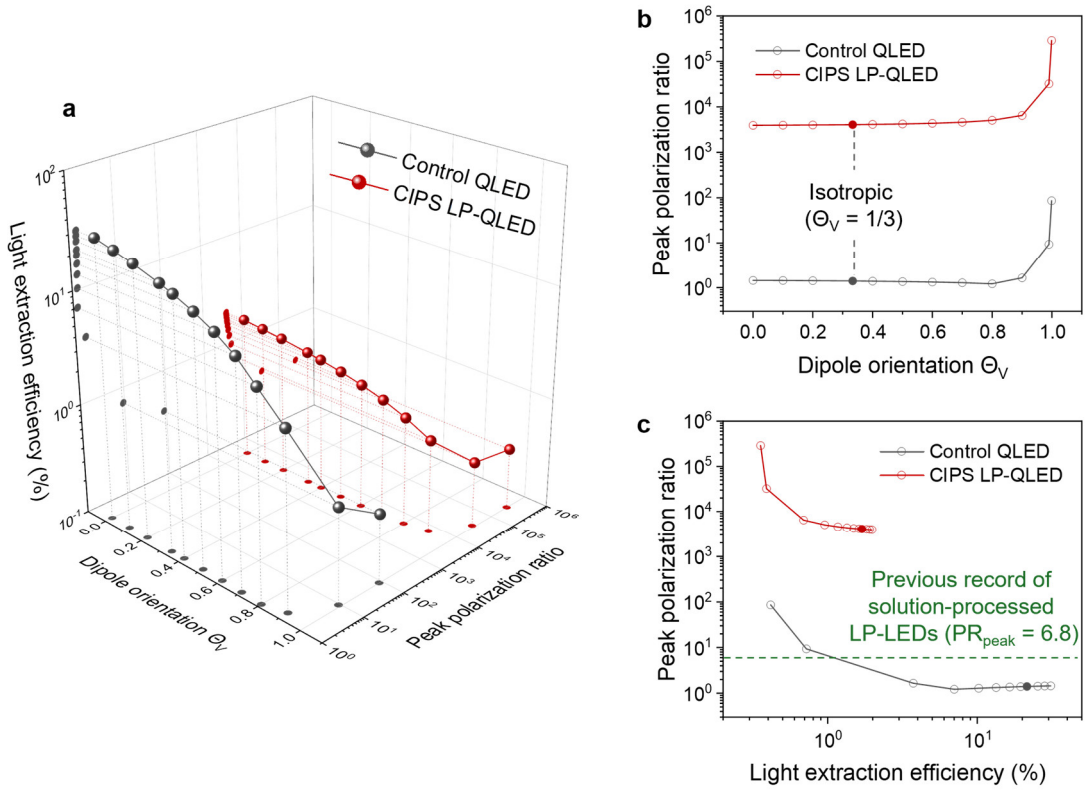

Figure S4. Comparative analysis of the type-B CIPS LP-QLED platform versus the traditional TDM manipulation in control QLED. (a) A 3D plot visualizing the performance landscape, comparing the LEE and peak PR as a function of the emitter's TDM orientation Θ_V for the CIPS-enabled LP-QLED (red) and control QLED (black). (b) A 2D projection showing peak PR as a function of Θ_V, highlighting the CIPS platform's ability to achieve exceptionally high PR across all TDM orientations, in contrast to the control QLED. (c) A 2D projection showing the direct trade-off between LEE and peak PR. The CIPS platform (red) operates in a performance regime superior to that of the TDM manipulation approach (black), far exceeding the previous experimental record for solution-processed LP-LEDs (peak PR ~6.8[4]).

As established in the main text and Note S1, the prevailing strategy for creating LP-LEDs relies on controlling the TDM orientation of anisotropic emitters. This material-centric approach, however, is bound by a severe, intrinsic trade-off between the PR and LEE. Specifically, within a standard device architecture, a meaningful peak PR (>10) is only achievable when the fraction of vertical dipoles Θ_V approaches unity ($\Theta_V \geq 0.99$). This requirement not only necessitates exceptionally challenging materials synthesis and processing to achieve near-perfect dipole alignment but also fundamentally limits the LEE to less than 0.8%. This inherent dilemma is a primary reason why the record PR for solution-processed LP-LEDs has remained limited (6.8[4]), lagging far behind their epitaxial[12] and organic[13] counterparts.

In contrast, the CIPS platform developed in this work effectively decouples the pursuit of a high PR from the difficult tasks of anisotropic material synthesis and TDM alignment. By shifting the origin of polarization from the emitter to the optical microcavity, the CIPS approach demonstrates remarkable general applicability, showing high performance with emitters ranging from perfectly horizontal ($\Theta_V = 0$) to perfectly vertical ($\Theta_V = 1$), including the macroscopically isotropic QDs with $\Theta_V \sim 1/3$ used in our devices.

While the CIPS platform also exhibits a trade-off between LEE and PR (as shown in Figs. 4c and S4), it operates in a performance regime vastly superior to that of the traditional TDM manipulation method. A comprehensive comparison of the two strategies is presented in Fig. S4. Although the control QLED can theoretically achieve a higher maximum LEE, this only occurs in a nearly unpolarized state (Fig. S4a). The superiority of the CIPS platform becomes evident when considering the achievable PR. As shown in Fig. S4b, the CIPS LP-QLED consistently yields a theoretical peak PR exceeding 3000 for any TDM orientation. In contrast, the control QLED only begins to show a PR greater than 9 when $\Theta_V \geq 0.99$, a regime of extreme and often impractical material engineering. For isotropic QDs ($\Theta_V \sim 1/3$), the control device is nearly unpolarized, with a peak PR of only ~1.4.

The most critical comparison is the direct relationship between LEE and peak PR, shown in Fig. S4c. While the control QLED offers a high LEE for low Θ_V values ($\Theta_V \leq 0.9$), it does so at the cost of a negligible PR. In the regime where the control device can produce any meaningful polarization (e.g., a peak PR of ~9 at $\Theta_V = 0.99$), its LEE has already plummeted to just 0.72%. For a given LEE, the CIPS platform would yield a PR two to three orders of magnitude higher. For example, using near-isotropic QDs ($\Theta_V \sim 1/3$), the CIPS device achieves a theoretical peak PR of ~3952 with an LEE of ~1.7%. Even for a completely horizontal emitter ($\Theta_V = 0$), the CIPS device still provides a peak PR of ~3920 with a respectable LEE of ~2.0%.

In conclusion, the CIPS platform can improve the overall performance of LP-LEDs by overcoming previous limitations. It not only eliminates the need for challenging TDM engineering for anisotropic emitters but also provides a superior balance between PR and LEE, enabling the use of readily available isotropic emitters to achieve state-of-the-art polarization performance.

Note S4. Theoretical framework and physical origin of the CIPS Effect, and MATLAB code.

The CIPS effect originates from the angle- and polarization-dependent optical response of the complete vertical microcavity, which includes the top Al mirror, the bottom DBR, and all intermediate functional layers in QLED. However, the dominant contribution to the polarization splitting itself comes from the DBR. The Al mirror has a relatively weak polarization dependence at the high angles of interest (see Fig. S11), and the thin carrier transport and QDs layers primarily contribute to the overall phase thickness of the cavity. Therefore, to elucidate the fundamental physical origin of the CIPS effect in the clearest possible way, it is sufficient and instructive to analyze the optical properties of the DBR in isolation. By studying how the DBR alone interacts with TE and TM polarized light, we can derive the essential physics of the polarization-dependent band-edge shift, which is the core mechanism exploited in our device. This DBR-centric model provides a direct and quantitative understanding of the splitting phenomenon, which is the foundation upon which the full device performance is built.

We model the DBR as an infinite periodic stack of two alternating dielectric layers: a high-index layer (H) with refractive index n_H and thickness d_H, and a low-index layer (L) with n_L and d_L. The analysis begins with the transfer matrix method (TMM).

For a plane wave of angular frequency ω propagating through a layer j, the electric (E_0) and magnetic (H_0) field at its front interface ($z = 0$) and back interface ($z = d_j$) are related by a characteristic matrix $\mathbf{M}_j$:

$$\begin{pmatrix} E_0 \\ H_0 \end{pmatrix} = \mathbf{M}_j \begin{pmatrix} E_d \\ H_d \end{pmatrix} = \begin{pmatrix} \cos\delta_j & \dfrac{i}{\eta_j}\sin\delta_j \\ i\eta_j \sin\delta_j & \cos\delta_j \end{pmatrix} \begin{pmatrix} E_d \\ H_d \end{pmatrix} \tag{1}$$

The phase thickness δ_j is given by

$$\delta_j = k_{z,j} d_j$$

where $k_{z,j}$ is the wavevector component normal to the interface:

$$k_{z,j} = \sqrt{\left(n_j \omega / c\right)^2 - k_x^2} \tag{2}$$

Here, $k_x = k_0 n_0 \sin\theta_0$ is the in-plane wavevector, which is conserved across all layers. The optical admittance η_j is the crucial polarization-dependent term. For TE waves, the electric field is perpendicular to the plane of incidence. The admittance is:

$$\eta_{j,TE} = \frac{k_{z,j}}{\omega \mu_0} \tag{3}$$

For TM waves, the magnetic field is perpendicular to the plane of incidence. The admittance is:

$$\eta_{j,TM} = \frac{n_j^2 \omega \varepsilon_0}{k_{z,j}} \tag{4}$$

A DBR unit cell consists of an H-L pair. Its transfer matrix is the product of the individual matrices:

$$\mathbf{M}_{unit} = \mathbf{M}_H \mathbf{M}_L = \begin{pmatrix} \cos\delta_H & \frac{i}{\eta_H}\sin\delta_H \\ i\eta_H \sin\delta_H & \cos\delta_H \end{pmatrix} \begin{pmatrix} \cos\delta_L & \frac{i}{\eta_L}\sin\delta_L \\ i\eta_L \sin\delta_L & \cos\delta_L \end{pmatrix}$$

Multiplying these matrices gives:

$$\mathbf{M}_{unit} = \begin{pmatrix} \cos\delta_H \cos\delta_L - \frac{\eta_L}{\eta_H}\sin\delta_H \sin\delta_L & i\left(\frac{\sin\delta_H \cos\delta_L}{\eta_H} + \frac{\cos\delta_H \sin\delta_L}{\eta_L}\right) \\ i\left(\eta_H \sin\delta_H \cos\delta_L + \eta_L \cos\delta_H \sin\delta_L\right) & \cos\delta_H \cos\delta_L - \frac{\eta_H}{\eta_L}\sin\delta_H \sin\delta_L \end{pmatrix} \quad (5)$$

For a wave propagating in an infinite periodic structure, the fields after one period ($\Lambda = d_H + d_L$) must be related to the initial fields by a Bloch phase factor $e^{\pm iK\Lambda}$, where K is the Bloch wavevector. This means $e^{\pm iK\Lambda}$ must be the eigenvalues of the unit cell matrix $\mathbf{M}_{\text{unit}}$. The sum of the eigenvalues is equal to the trace of the matrix, $Tr(\mathbf{M}_{\text{unit}})$.

$$e^{iK\Lambda} + e^{-iK\Lambda} = Tr(\mathbf{M}_{\text{unit}})$$

From Euler's formula and Equation (5), we can get:

$$2\cos(K\Lambda) = m_{11} + m_{22} = 2\cos\delta_H \cos\delta_L - \left(\frac{\eta_L}{\eta_H} + \frac{\eta_H}{\eta_L}\right)\sin\delta_H \sin\delta_L$$

$$\cos(K\Lambda) = \cos\delta_H \cos\delta_L - \frac{1}{2}\left(\frac{\eta_L}{\eta_H} + \frac{\eta_H}{\eta_L}\right)\sin\delta_H \sin\delta_L \quad (6)$$

This is the dispersion relation for the infinite DBR.

The photonic stopband (the high-reflectivity band) exists when the wave cannot propagate, meaning the Bloch wavevector K is complex. This occurs when $|\cos(K\Lambda)| > 1$. The band edges are precisely where $|\cos(K\Lambda)| = 1$.

Let's examine the polarization-dependent term in Equation (6):

$$X_{pol} = \frac{1}{2}\left(\frac{\eta_H}{\eta_L} + \frac{\eta_L}{\eta_H}\right)$$

Substituting the definitions of admittance for each polarization (normalized for simplicity):

For TE modes:

$$X_{TE} = \frac{1}{2}\left(\frac{n_H \cos\theta_H}{n_L \cos\theta_L} + \frac{n_L \cos\theta_L}{n_H \cos\theta_H}\right) \quad (7)$$

This term depends on the cosine of the propagation angles.

For TM modes:

$$X_{TM} = \frac{1}{2}\left(\frac{n_H / \cos\theta_H}{n_L / \cos\theta_L} + \frac{n_L / \cos\theta_L}{n_H / \cos\theta_H}\right) = \frac{1}{2}\left(\frac{n_H \cos\theta_L}{n_L \cos\theta_H} + \frac{n_L \cos\theta_H}{n_H \cos\theta_L}\right) \quad (8)$$

This term depends on a ratio involving the inverse of the cosines.

At normal incidence ($\theta_j = 0$, $\cos\theta_j = 1$), $X_{TE} = X_{TM}$, so the dispersion relations are identical, and the stopbands do not split. However, for any non-normal incidence ($\theta_j > 0$, $\cos\theta_j < 1$), the values of X_{TE} and X_{TM} diverge. Since the band-edge condition depends directly on these terms, the spectral positions of the stopband edges for TE and TM modes will diverge. This differential shift, which increases with the angle of incidence, is the quantitative origin of the CIPS effect.

Below is the MATLAB code for CIPS analysis on DBR:

```
% --- MATLAB script for detailed DBR analysis ---
% This script analyzes a DBR stack assuming incident from air, by:
% 1. Plotting angle-resolved reflectance spectra with band edges overlaid.
% 2. Analyzing and plotting the splitting of the photonic stopband edges and center.
% 3. Calculating and plotting the transmittance at 537 nm vs. angle.

clear; clc; close all;

%% --- 1. Define simulation and DBR parameters ---
lambda_range_nm = 400:0.5:700;      % Wavelength range for spectra (nm)
theta_deg = 0:0.5:85;             % Incident angle range (degrees)
theta_rad = deg2rad(theta_deg);    % Incident angle in radians

% --- Material dispersion data (wavelengths in nm) ---
lambda_high_nm = [310, 410, 510, 610, 710, 810];
n_high_data = [2.51652, 2.29018, 2.21599, 2.18412, 2.16784, 2.15847]; % Ta2O5
lambda_low_nm = [310, 410, 510, 610, 710, 810];
n_low_data = [1.48534, 1.46911, 1.4618, 1.45777, 1.45509, 1.45325]; % SiO2

% Create interpolation functions for refractive indices
n_H_func = @(l) interp1(lambda_high_nm, n_high_data, l, 'pchip');
n_L_func = @(l) interp1(lambda_low_nm, n_low_data, l, 'pchip');

% --- DBR stack definition ---
n_incident = 1.0;  % Refractive index of incident medium (air)
n_exit = 1.46;     % Refractive index of exit medium (quartz substrate)
d_H = 66.3;        % Thickness of Ta2O5 (nm)
d_L = 99.4;        % Thickness of SiO2 (nm)
num_pairs = 16;

% Pre-allocate matrices
R_tm = zeros(length(lambda_range_nm), length(theta_rad));
R_te = zeros(length(lambda_range_nm), length(theta_rad));

%% --- 2. TMM calculation loop ---
for i_lam = 1:length(lambda_range_nm)
    lambda_nm = lambda_range_nm(i_lam);
    n_H = n_H_func(lambda_nm);
    n_L = n_L_func(lambda_nm);
    for i_ang = 1:length(theta_rad)
        theta0 = theta_rad(i_ang);
```

```
        R_tm(i_lam, i_ang) = calculate_DBR_reflectance(lambda_nm, theta0, 'tm',
n_incident, n_exit, n_H, n_L, d_H, d_L, num_pairs);
        R_te(i_lam, i_ang) = calculate_DBR_reflectance(lambda_nm, theta0, 'te',
n_incident, n_exit, n_H, n_L, d_H, d_L, num_pairs);
    end
end

%% --- 3. Band-edge and splitting analysis ---
reflectance_threshold = 0.8;
upper_edge_tm = NaN(size(theta_deg)); lower_edge_tm = NaN(size(theta_deg));
upper_edge_te = NaN(size(theta_deg)); lower_edge_te = NaN(size(theta_deg));

for i_ang = 1:length(theta_deg)
    [upper_edge_tm(i_ang), lower_edge_tm(i_ang)] = find_band_edges(R_tm(:, i_ang),
lambda_range_nm, reflectance_threshold);
    [upper_edge_te(i_ang), lower_edge_te(i_ang)] = find_band_edges(R_te(:, i_ang),
lambda_range_nm, reflectance_threshold);
end

splitting_upper = upper_edge_tm - upper_edge_te;
splitting_lower = lower_edge_tm - lower_edge_te;
splitting_center = (upper_edge_tm + lower_edge_tm)/2 - (upper_edge_te +
lower_edge_te)/2;

%% --- 4. Visualization ---
% Figure 1: DBR angle-resolved reflectance spectra with band-edges
figure('Name', 'Figure 1: DBR reflectance with band-edges', 'Position', [50, 600, 1200,
400]);
% TM Plot
subplot(1, 2, 1);
imagesc(theta_deg, lambda_range_nm, R_tm);
set(gca, 'YDir', 'normal'); colorbar; colormap('jet'); caxis([0 1]);
hold on;
plot(theta_deg, lower_edge_tm, 'w--', 'LineWidth', 1.5, 'DisplayName', 'TM band-edge');
plot(theta_deg, upper_edge_tm, 'w--', 'LineWidth', 1.5, 'HandleVisibility', 'off');
xlabel('Incident angle \theta_{in} (°)'); ylabel('Wavelength (nm)'); title('TM
reflectance');
yline(537, '--k', 'LineWidth', 1.5);
set(gca, 'FontSize', 12);

% TE Plot
subplot(1, 2, 2);
imagesc(theta_deg, lambda_range_nm, R_te);
set(gca, 'YDir', 'normal'); colorbar; colormap('jet'); caxis([0 1]);
hold on;
plot(theta_deg, lower_edge_te, 'w--', 'LineWidth', 1.5, 'DisplayName', 'TE Band Edge');
plot(theta_deg, upper_edge_te, 'w--', 'LineWidth', 1.5, 'HandleVisibility', 'off');
xlabel('Incident angle \theta_{in} (°)'); ylabel('Wavelength (nm)'); title('TE
reflectance');
yline(537, '--k', 'LineWidth', 1.5);
set(gca, 'FontSize', 12);
```

```
 sgtitle('Angle-resolved reflectance of DBR with band-edges overlaid', 'FontWeight',
'bold');


 % Figure 2: Transmittance at 537 nm (QD EL peak)
 target_lambda = 537;
 [~, lambda_idx] = min(abs(lambda_range_nm - target_lambda));
 T_tm_537 = 1 - R_tm(lambda_idx, :); % T = 1 - R (assuming lossless)
 T_te_537 = 1 - R_te(lambda_idx, :);

 figure('Name', 'Figure 2: Transmittance', 'Position', [100, 100, 700, 500]);
 plot(theta_deg, T_tm_537 * 100, 'r-', 'LineWidth', 2, 'DisplayName', 'TM Mode');
 hold on;
 plot(theta_deg, T_te_537 * 100, 'b-', 'LineWidth', 2, 'DisplayName', 'TE Mode');
 grid on; xlabel('Emission angle \theta_{em} (°)'); ylabel('Transmittance (%)');
 title(['Transmittance at ' num2str(target_lambda) ' nm']);
 legend('show', 'Location', 'northwest'); set(gca, 'FontSize', 12); ylim([-5 105]);

 % Figure 3: Band-edge and center splitting analysis
 figure('Name', 'Figure 3: Splitting analysis', 'Position', [850, 100, 700, 500]);
 plot(theta_deg, splitting_upper, 'r-', 'LineWidth', 2, 'DisplayName', 'Upper edge
splitting (\Delta\lambda_{14})');
 hold on;
 plot(theta_deg, splitting_lower, 'b-', 'LineWidth', 2, 'DisplayName', 'Lower edge
splitting (\Delta\lambda_{lower})');
 plot(theta_deg, splitting_center, 'k--', 'LineWidth', 2, 'DisplayName', 'Center
wavelength splitting (\Delta\lambda_{center})');
 grid on; xlabel('Incident angle \theta_{in} (°)'); ylabel('Wavelength Splitting (nm)');
 title('TM-TE stopband splitting analysis');
 legend('show', 'Location', 'northwest'); set(gca, 'FontSize', 12);

 %% --- TMM function for DBR reflectance ---
 function R = calculate_DBR_reflectance(lambda_nm, theta0_rad, polarization, n_incident,
n_exit, n_H, n_L, d_H, d_L, num_pairs)
     N = n_incident; d_nm = inf;
     for i = 1:num_pairs
         N = [N, n_H, n_L];
         d_nm = [d_nm, d_H, d_L];
     end
     N = [N, n_exit]; d_nm = [d_nm, inf];

     film_indices = 2:(length(N)-1);
     M_total = eye(2);
     for j = film_indices
         Nj = N(j); dj = d_nm(j);
         cos_theta_j = sqrt(1 - (N(1)/Nj * sin(theta0_rad))^2);
         delta_j = (2*pi/lambda_nm) * Nj * dj * cos_theta_j;
         if strcmpi(polarization, 'tm'), eta_j = Nj / cos_theta_j; else, eta_j = Nj *
cos_theta_j; end
         Mj = [cos(delta_j), 1i/eta_j * sin(delta_j); 1i*eta_j * sin(delta_j),
cos(delta_j)];
```

```
        M_total = M_total * Mj;
    end
    cos_theta_s = sqrt(1 - (N(1)/N(end) * sin(theta0_rad))^2);
    if strcmpi(polarization, 'tm'), eta_0 = N(1) / cos(theta0_rad); eta_s = N(end) /
cos_theta_s;
    else, eta_0 = N(1) * cos(theta0_rad); eta_s = N(end) * cos_theta_s; end
    m11=M_total(1,1); m12=M_total(1,2); m21=M_total(2,1); m22=M_total(2,2);
    r_num = (eta_0 * m11 + eta_0 * eta_s * m12) - (m21 + eta_s * m22);
    r_den = (eta_0 * m11 + eta_0 * eta_s * m12) + (m21 + eta_s * m22);
    r = r_num / r_den;
    R = abs(r)^2;
 end

 function [upper_edge, lower_edge] = find_band_edges(R_spectrum, lambda_vector,
threshold)
    above_threshold = R_spectrum >= threshold;
    edges = find(diff([0; above_threshold; 0]));
    if numel(edges) < 2, upper_edge = NaN; lower_edge = NaN; return; end
    [~, max_idx] = max(edges(2:2:end) - edges(1:2:end-1));
    start_idx = edges(2*max_idx - 1);
    end_idx = edges(2*max_idx) - 1;
    lower_edge = lambda_vector(start_idx);
    upper_edge = lambda_vector(end_idx);
 end
```

Figure S5. Photoluminescence (PL) and electroluminescence (EL) characteristics of QDs with CdZnSe/ZnSe/$Zn_xCd_{1-x}S$ core/graded layer/shell structure and control QLED.

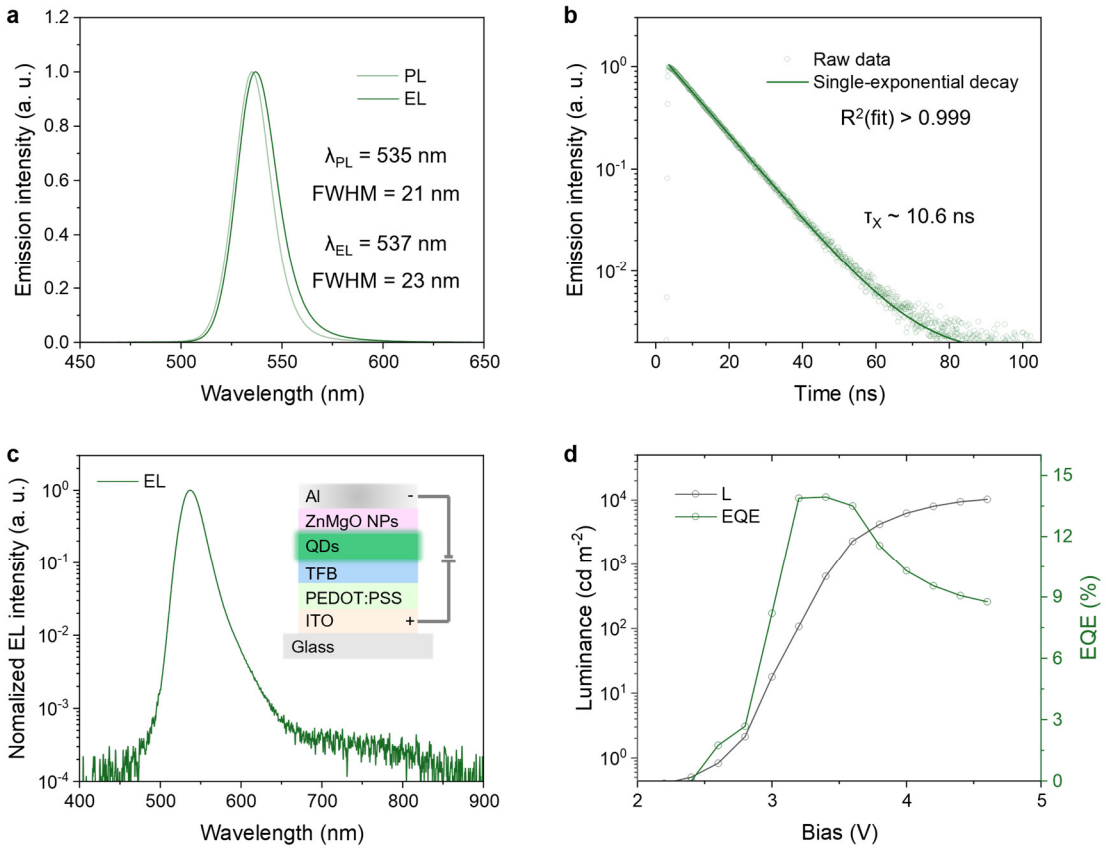

(a) Normalized PL spectrum of the QDs on quartz and the EL spectrum of the control QLED under a 3.5 V bias.

(b) Time-resolved PL (TRPL) decay of the QDs. The single-exciton PL lifetime (τ_X) is 10.6 ns. The near-single-exponential decay, with a coefficient of determination (R^2) > 0.999, indicates a near-unity photoluminescence quantum yield (PLQY) [15].

(c) Normalized EL spectrum from (a) on a logarithmic scale. The inset shows the device architecture of the control QLED.

(d) Measured luminance and external quantum efficiency (EQE) of the control QLED as a function of applied bias. The device achieves a peak EQE of approximately 14%.

Figure S6. Transmission electron microscopy (TEM) images of QDs and analysis of QD diameter distribution.

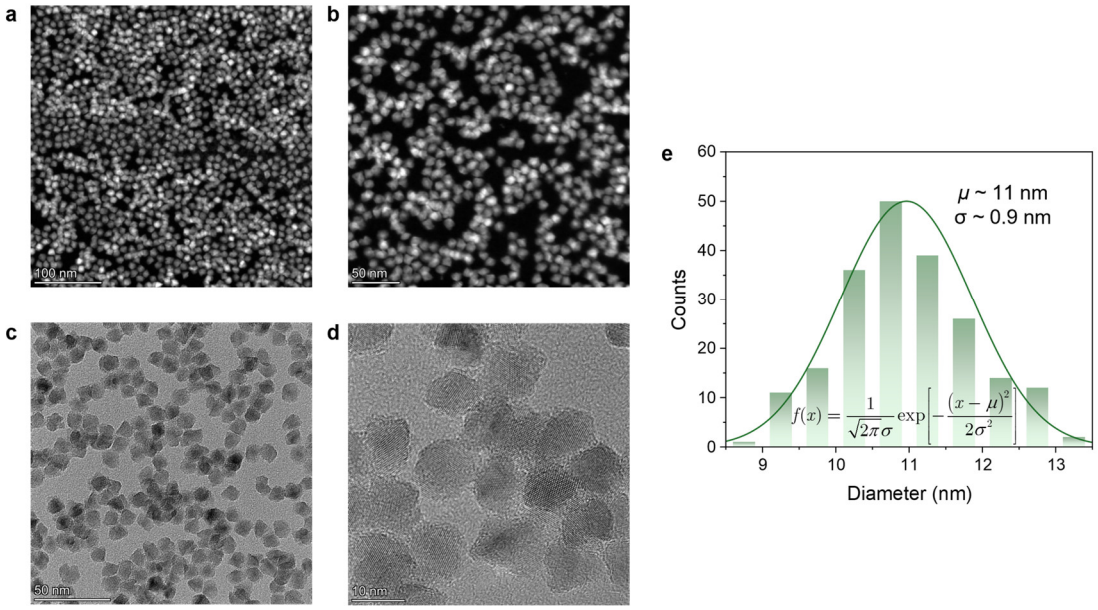

(a, b) Dark-field and (c, d) bright-field TEM images of the QDs.

(e) Histogram of the QD diameter distribution. The solid line represents a Gaussian fit, where the mean diameter (μ) and standard deviation (σ) are determined to be 11 nm and 0.9 nm, respectively, demonstrating a pronounced monodispersity of the QDs.

Figure S7. Back focal plane (BFP) imaging of QDs film on glass.

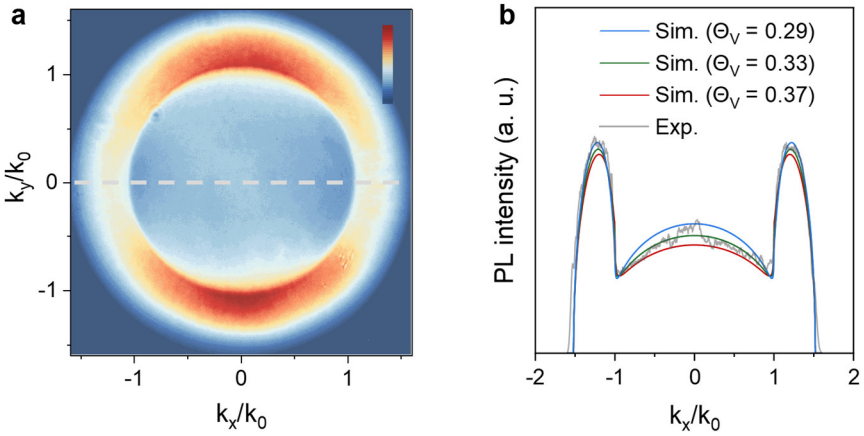

(a) Experimental BFP image of the QDs film on glass.

(b) Comparison of the experimental PL intensity profile (extracted along the dashed line in Fig. S7a) with simulation results. Fitting yields a Θ_V of ~0.33, indicative of a macroscopic isotropic TDM distribution in the QDs film on glass.

Figure S8. The structure of three types of QLEDs: control QLED, type-A and type-B LP-QLEDs.

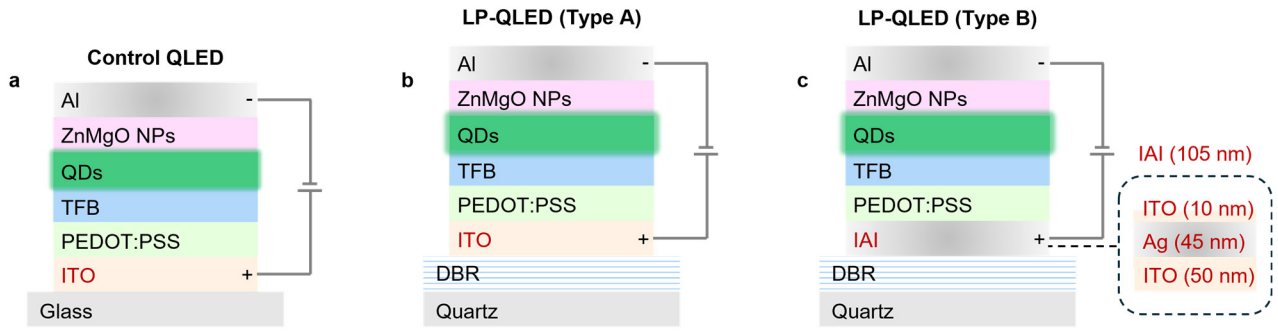

d

Layer	Control QLED	LP-QLED (Type A)	LP-QLED (Type B)
Substrate	Glass (1 mm)	Quartz (1 mm)	
DBR	/	16 pairs of Ta_2O_5 (66.3 nm for each layer)/SiO_2 (99.4 nm for each layer)	
Anode	ITO (100 nm)	ITO (85 nm)	IAI (50 nm ITO + 45 nm Ag + 10 nm ITO)
Hole injection layer (HIL)	PEDOT:PSS (30 nm)		
Hole transport layer (HTL)	TFB (30 nm)		
Emissive layer (EML)	QDs (22 nm)		
Electron transport layer (ETL)	ZnMgO NPs (45 nm)		
Cathode	Al (100 nm)		

Schematic of the device structures for the (a) control QLED, (b) type-A LP-QLED, and (c) type-B LP-QLEDs.

(d) A summary of the functional layers and corresponding layer thicknesses for each device configuration.

Figure S9. Experimental setup for polarization- resolved PL and EL measurement.

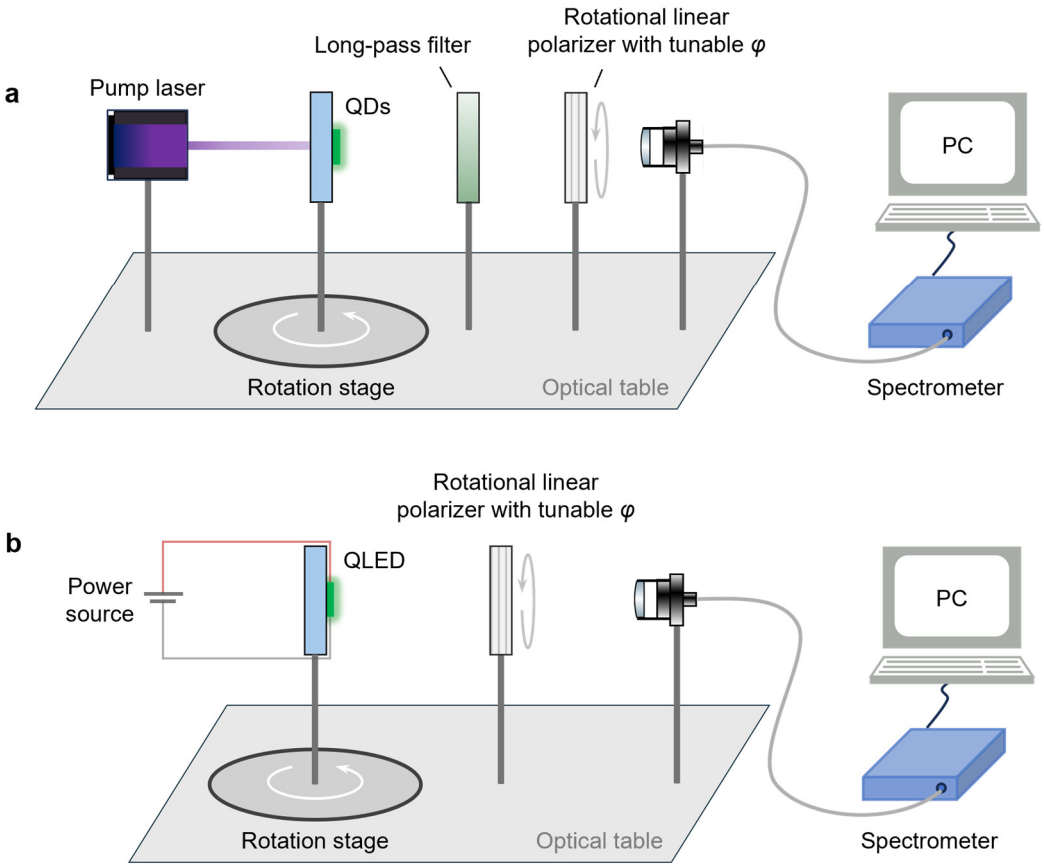

(a) Schematic of the experimental setup for polarization-resolved PL measurement. The sample is mounted on a rotation stage to control the emission angle θ and is excited by a 355 nm laser (CNI, MPL-FN-355). A long-pass filter with cut-on wavelength of 405 nm blocks the pump laser, followed by a rotational linear polarizer (LBTEK, FLP25-VIS-M, with a high extinction ratio above 10000 at green and red wavelengths) to select the polarization angle φ. The signal is then collected and analyzed by a high-sensitivity spectrometer (Flight, FLA6500) and a PC connected to it.

(b) Schematic of the experimental setup for polarization-resolved EL measurement. The setup is analogous to the PL system, where the sample is an electrically driven QLED, and consequently, the pump laser and long-pass filter are removed.

Figure S10. Refractive indices of the materials involved in this work.

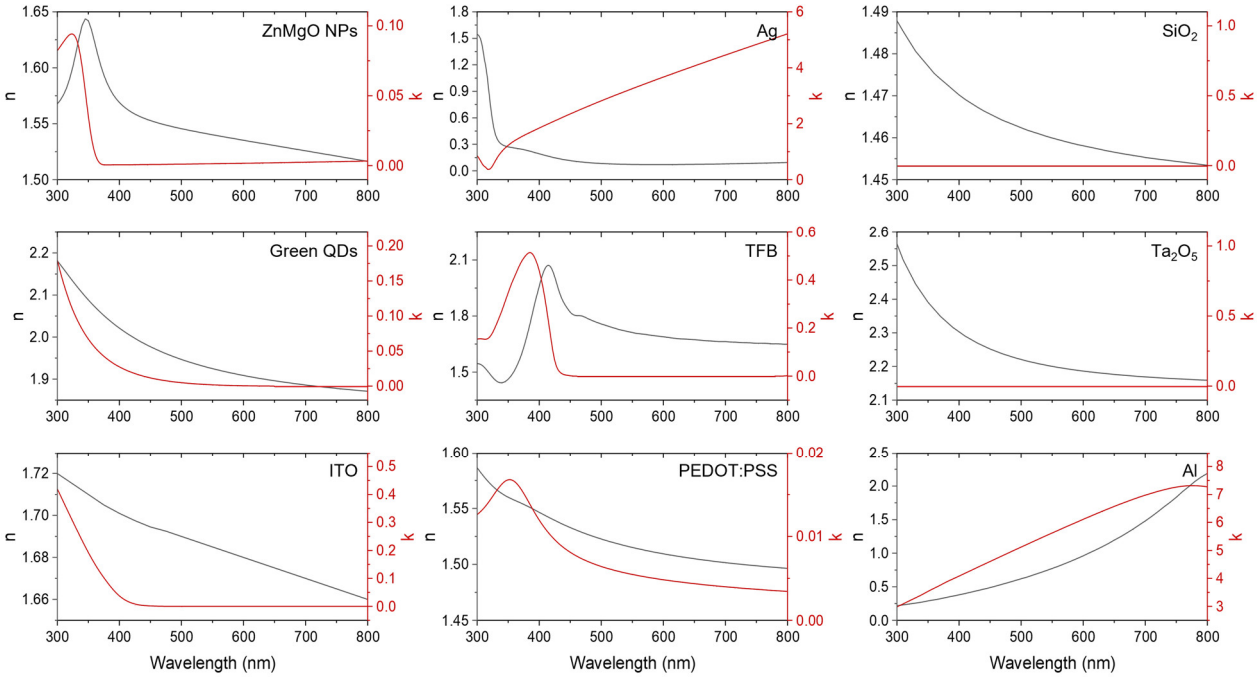

The refractive indices (*n* and *k*) of above materials are characterized by ellipsometer (TF-UVISEL, Horiba).

Figure S11. Simulated angle-resolved reflectance spectrum of the 16-pair Ta_2O_5/SiO_2 DBR and 100-nm-thick aluminum thin film.

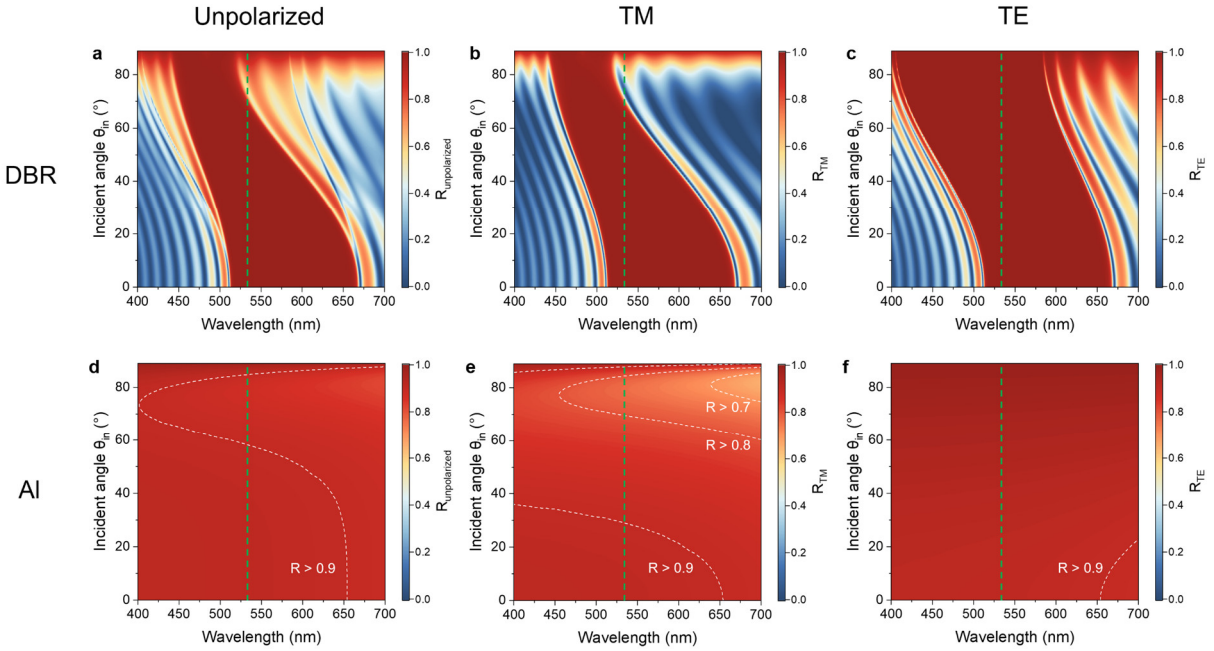

(a-c) Reflectance spectra of the 16-pair Ta_2O_5/SiO_2 DBR for (a) unpolarized, (b) TM-polarized, and (c) TE-polarized incident light with different θ_{in}.

(d-f) Reflectance spectra of a 100-nm-thick Al thin film for (d) unpolarized, (e) TM-polarized, and (f) TE-polarized incident light with different θ_{in}.

The green dashed lines indicate the peak EL wavelength (537 nm) of the control QLED.

Figure S12. Characterization of the 16-pair Ta_2O_5/SiO_2 DBR on quartz (normal incidence).

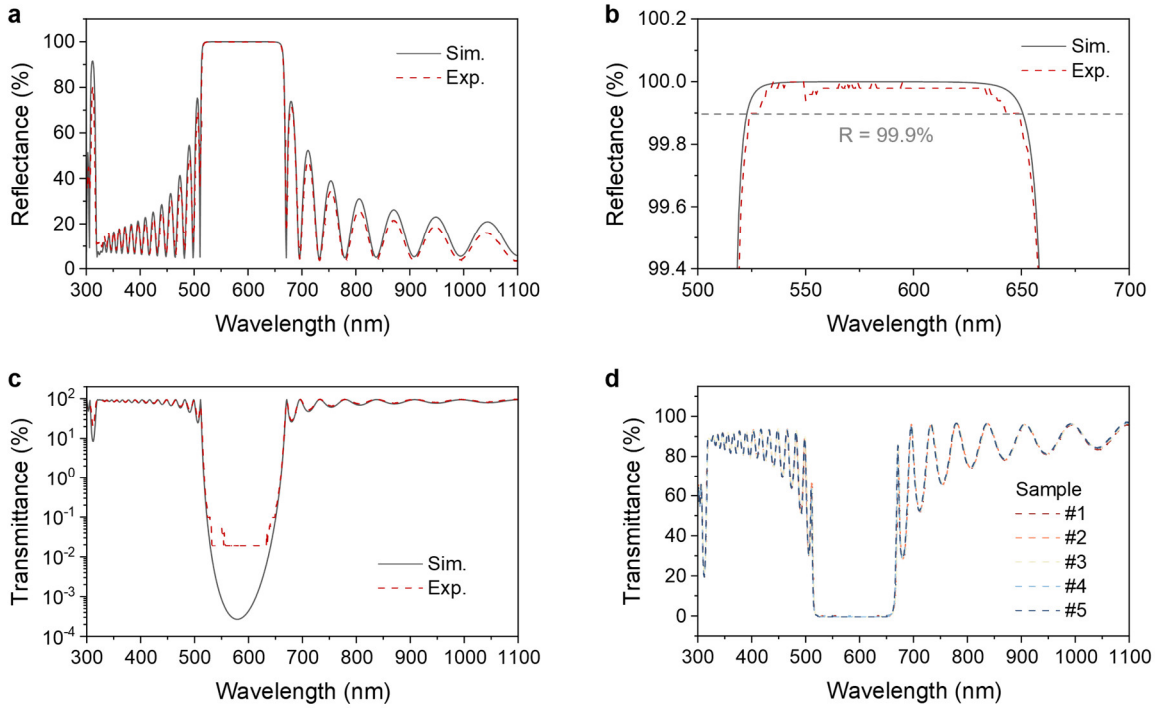

(a, b) A comparison between simulated (black solid curves) and experimentally measured (red dashed curves) spectra at normal incidence (incident angle $\theta_{in} = 0°$). The reflectance spectrum reveals a photonic stopband with a maximum reflectance (R_{max}) at ~579 nm. The measured high-reflectance ($\geq$ 99.9%) band spans from 524 to 649 nm.

(c) The transmission spectra, shown on a logarithmic scale, confirms a deep attenuation within the stopband.

(d) Transmission spectra from five fabricated DBR samples illustrate the high reproducibility of the DBR.

Figure S13. EL polarization characteristics of the type-A LP-QLED at various emission angles.

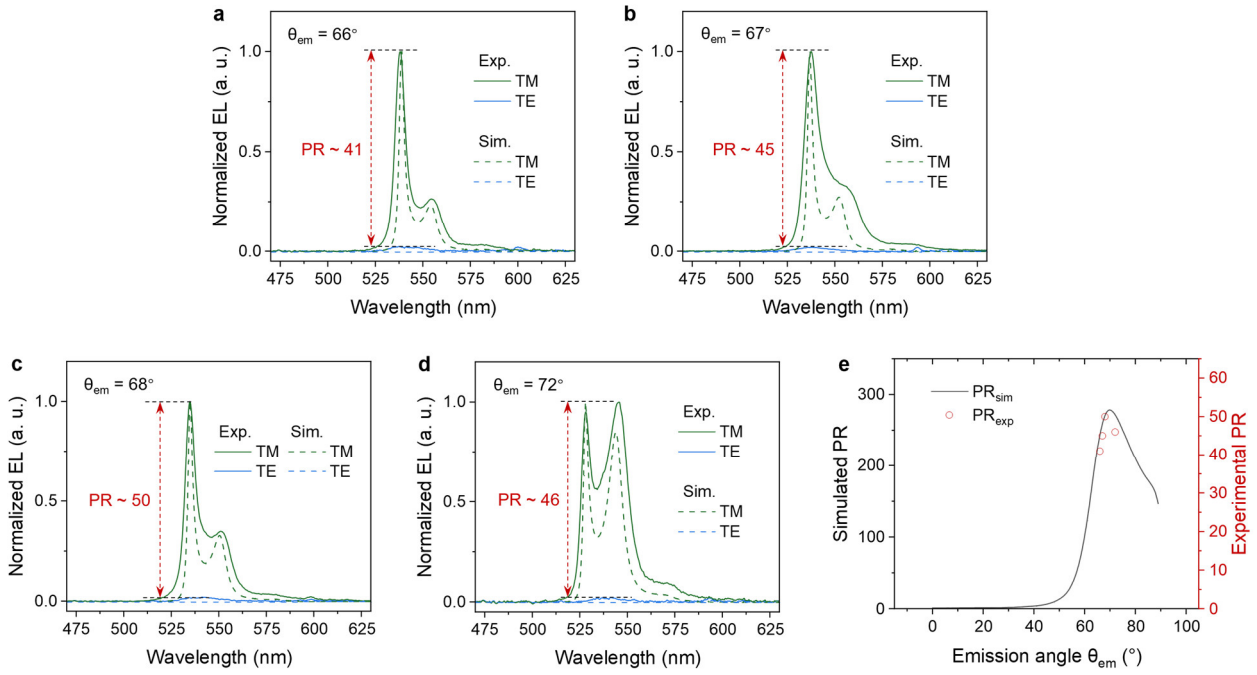

(a-d) Experimental (solid lines) and simulated (dashed lines) EL spectra for both TM and TE modes, measured at emission angles θ_{em} of (a) 66°, (b) 67°, (c) 68°, and (d) 72°. The corresponding experimental PR is indicated in each panel.

(e) θ_{em}-dependent simulated (solid line) and experimental (open circles) PR values, showing a peak near 70°.

Figure S14. Analysis of power dissipation and mode distribution in type-A LP-QLED.

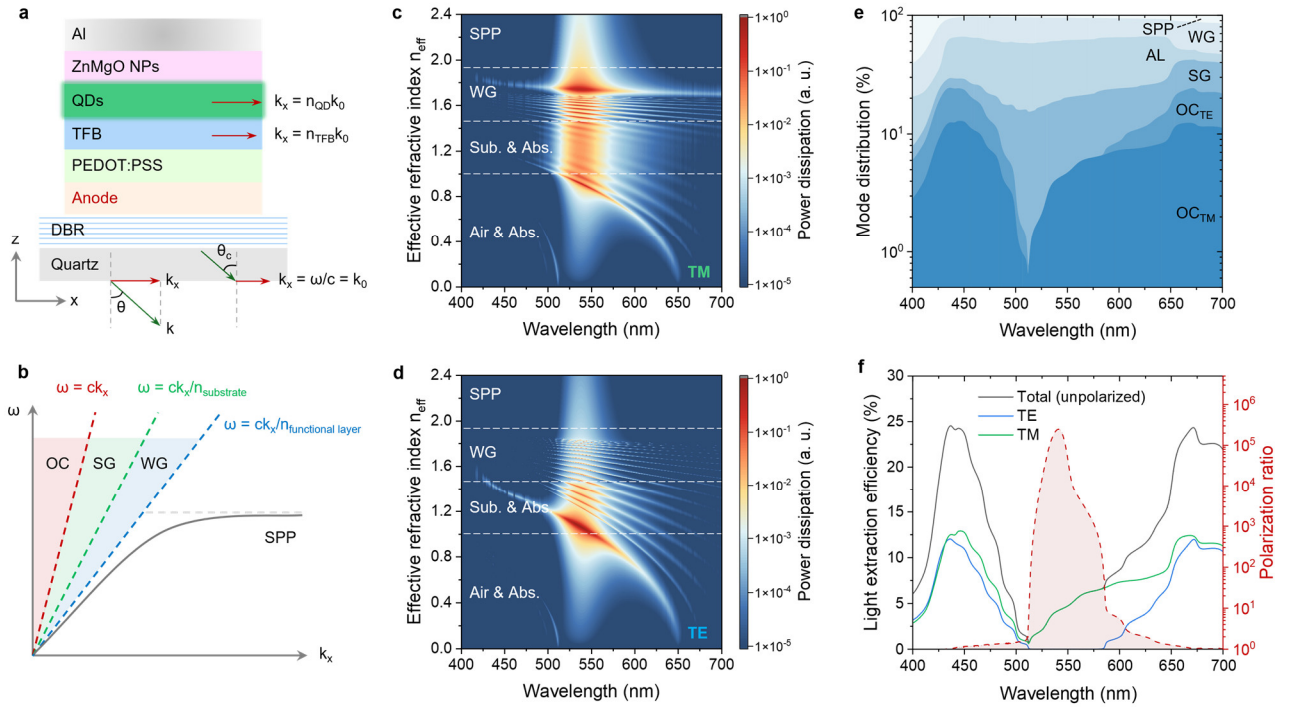

(a) Schematic cross-section of the type-A LP-QLED. The propagation of light is described by its wavevector k and the angle θ relative to the interface normal (z-axis). The in-plane component of the wavevector, k_x , is defined by

$$k_x = \left|\vec{k}\right| \sin\theta = nk_0 \sin\theta$$

where n is the refractive index of the medium and $k_0 = \omega/c$ is the wavevector in free space. ω and c are the angular frequency and velocity of light in vacuum, respectively. The k_x provides information on the propagation angle θ as well as the medium where the wave propagates both inside and outside of the LED. The analysis can be simplified by using the effective refractive index n_{eff}, which is defined by

$$n_{eff} = k_x / k_0 = n \sin\theta$$

(b) Schematic dispersion diagram (ω–k_x) for the LP-QLED, which is divided into distinct optical channels by light lines. The light lines represent the maximum possible in-plane wavevector k_x in a given medium (e.g., $\omega = ck_x/n_{medium}$), and they are used to distinguish each region in the dispersion diagram. Light that can escape into the air is termed the out-coupled (OC) mode, existing in the region where $0 \leq n_{eff} < 1$. Light that is trapped within the quartz substrate via total internal reflection (TIR) is the substrate-guided (SG) mode, occupying the region $1 \leq n_{eff} < n_{quartz}$ (where $n_{quartz} \approx 1.46$ at green wavelengths). Similarly, light confined within the high-index functional layers (e.g., ITO, PEDOT:PSS, TFB, QDs, ZnMgO NPs. The n for these materials at green wavelengths are approximately 1.69, 1.52, 1.72, 1.93, 1.54, respectively) by TIR constitutes the waveguide (WG) modes, which exist for $n_{quartz} \leq n_{eff} < n_{QD}$. Finally, surface plasmon polariton (SPP) modes are non-

radiative modes confined to the metal-dielectric interface, occurring at high in-plane wavevectors ($n_{eff} \geq n_{QD}$). The frequency-dependent wavevector for the SPP mode is given by

$$k_{SPP} = k_0\sqrt{\frac{\varepsilon_m\varepsilon_d}{\varepsilon_m + \varepsilon_d}} = \frac{\omega}{c}\sqrt{\frac{\varepsilon_m\varepsilon_d}{\varepsilon_m + \varepsilon_d}}$$

where ε_m is the complex dielectric function of the metal, and ε_d is the complex dielectric function of the dielectric layer attached to the metal. Since the SPP dispersion curve does not intersect the light lines, it cannot couple to radiative modes and are eventually dissipated as absorption losses in the metal cathode, representing a loss channel.

(c, d) Simulated power dissipation spectra as a function of wavelength and n_{eff} for (c) TM- and (d) TE-polarized light in the type-A LP-QLED. The power is distributed into the different optical channels defined by n_{eff}:

- $0 \leq n_{eff} < 1$: OC mode and associated absorption loss (AL) mode;
- $1 \leq n_{eff} < n_{quartz}$: SG mode and associated AL mode;
- $n_{quartz} \leq n_{eff} < n_{QD}$: WG mode in the functional layers (PEDOT:PSS, TFB, QDs, ZnMgO NPs);
- $n_{eff} \geq n_{QD}$: SPP mode.

(e) Wavelength-dependent mode distribution in type-A LP-QLED, summarizing the fraction of power coupled into each optical channel.

(f) Wavelength-dependent LEE for total unpolarized (black), TM-polarized (green), and TE-polarized (blue) light. The resulting polarization ratio (PR, red dashed line), calculated as LEE_{TM}/LEE_{TE}, is also plotted. In the green spectral region, the LEE_{TE} is strongly suppressed while the TM mode can be effectively extracted, leading to a large calculated PR that peaks at approximately 2.48×10^5 at 541 nm.

Figure S15. Comparison of the Purcell effect in type-A and type-B LP-QLEDs.

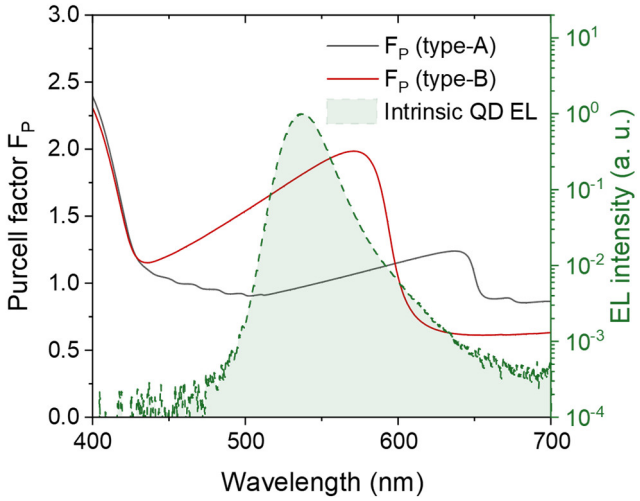

Simulated Purcell factor (F_P) as a function of wavelength for the type-A (solid black line) and type-B (solid red line) LP-QLEDs. The intrinsic EL spectrum of QDs in control QLED is given for reference (green shaded area).

The type-B device exhibits a significantly enhanced F_P (~1.81) compared to the type-A device (~0.97) at the primary green emission band. This enhancement of the spontaneous emission rate is crucial for maintaining high EL efficiency and brightness[16]. Additionally, the suppression of the F_P at off-peak red wavelengths in the type-B device contributes to higher emission color purity.

Figure S16. Comparison of simulated angle-dependent reflectance spectra for ITO-on-DBR and IAI-on-DBR.

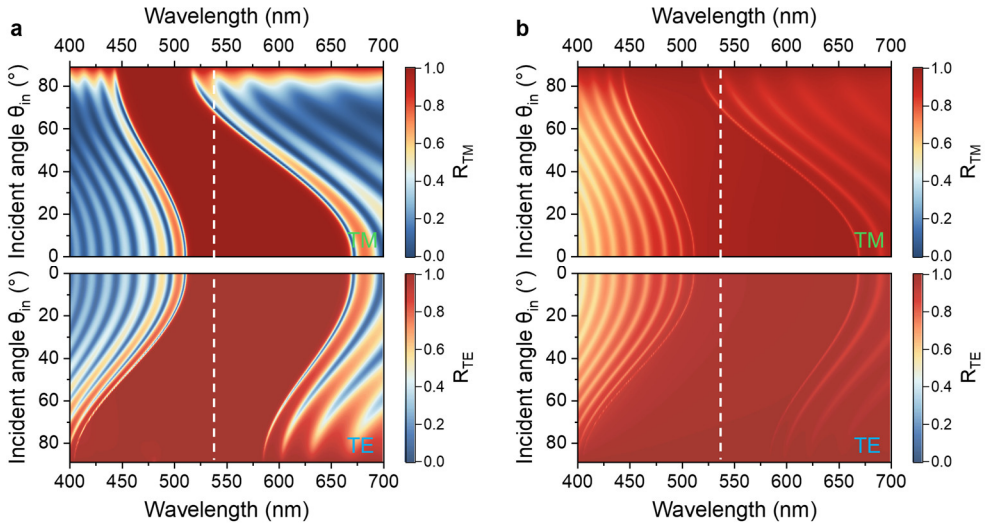

(a) Angle-resolved reflectance spectra for the type-A LP-QLED's ITO-on-DBR, showing TM (top) and TE (bottom) modes.

(b) Corresponding reflectance spectra for the type-B LP-QLED's IAI-on-DBR.

The comparison clearly shows that replacing the ITO with the IAI multilayer significantly broadens the high-reflectivity stopband for both polarizations across all incident angles θ_{in}. This enhancement is crucial for suppressing off-peak parasitic emission while maintaining the strong polarization splitting required for the CIPS effect. The white dashed lines indicate the QD's intrinsic EL peak at 537 nm.

Figure S17. Analysis of power dissipation and mode distribution in type-B LP-QLED.

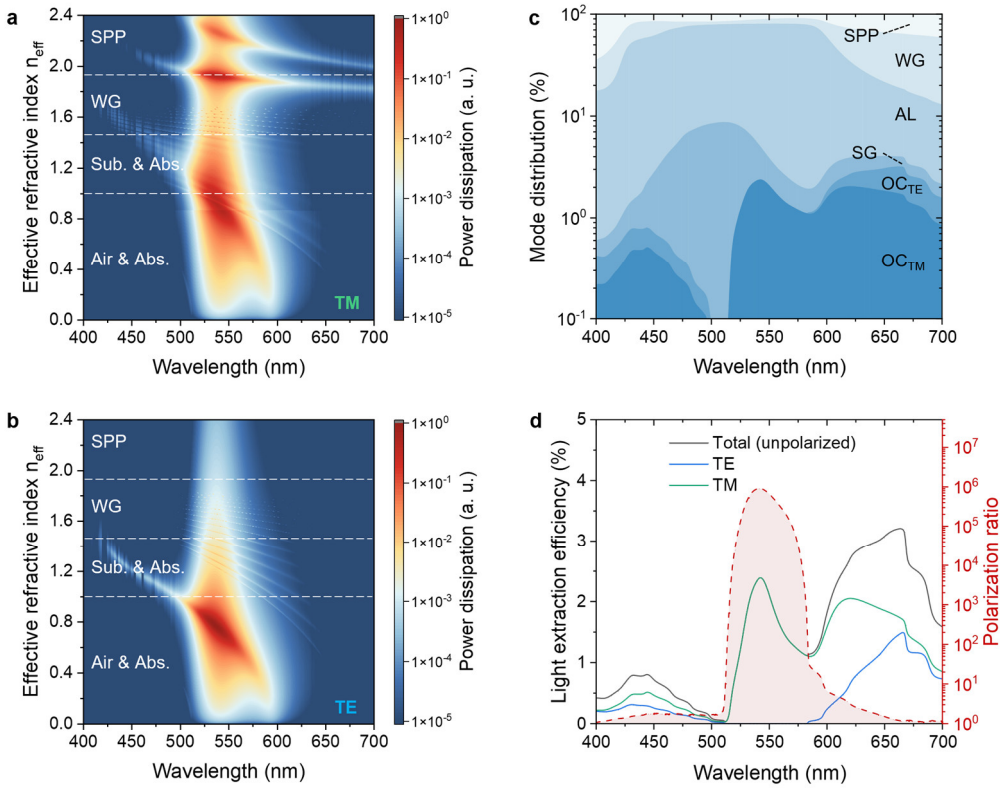

(a, b) Simulated power dissipation spectra as a function of wavelength and n_{eff} for (a) TM- and (b) TE-polarized light in the type-B LP-QLED.

(c) Wavelength-dependent mode distribution in type-B LP-QLED.

(d) Wavelength-dependent LEE for unpolarized (black), TM-polarized (green), and TE-polarized (blue) light. The wavelength-dependent PR curve (red dashed line) is also plotted. The calculated peak PR for the type-B device reaches approximately 9.11×10^5 at 541 nm, which is more than three times higher than the peak value of 2.48×10^5 for the type-A device (see in Fig. S14f).

Figure S18. Comparison of measured EL spectra for type-A and type-B LP-QLEDs.

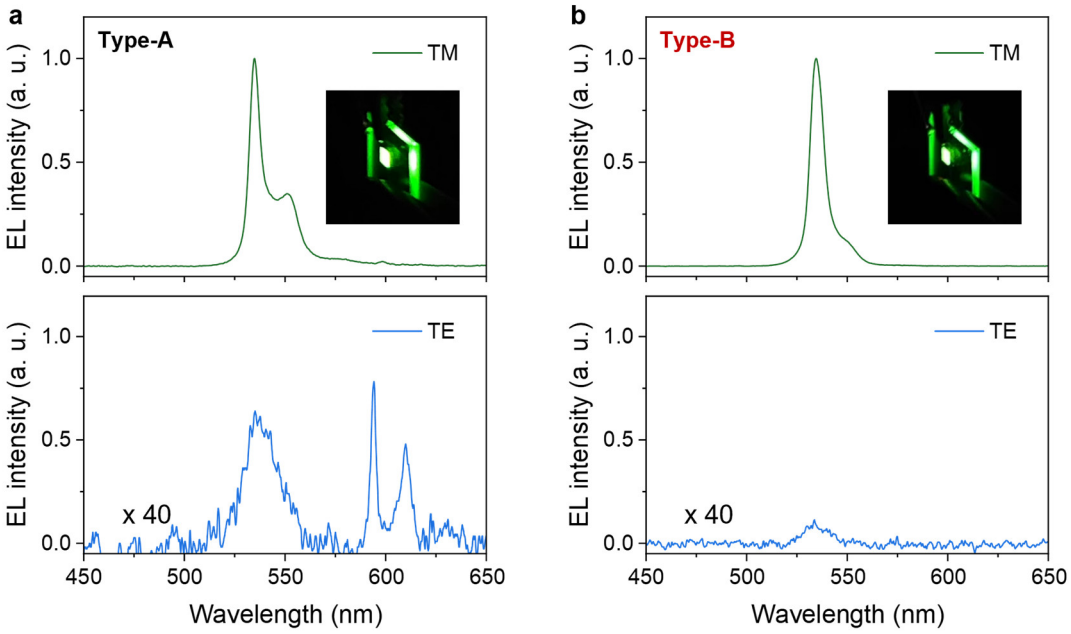

The figure contrasts the measured TM (top) and TE (bottom) polarized EL spectra for the (a) type-A at $\theta_{em} = 68°$ and (b) type-B LP-QLEDs at $\theta_{em} = 71°$. Insets show the LP-QLEDs operating under 3.5 V bias (active area is 0.04 cm^2). Note that the TE spectra in both panels are magnified by a factor of 40 for visibility.

The type-A device exhibits noticeable parasitic side peaks in its TM-polarized spectrum and a relatively strong TE-polarized emission. In contrast, the type-B device shows a significantly cleaner TM-polarized spectrum and a strongly suppressed TE-polarized emission, providing direct evidence for the effective mitigation of both parasitic emission and TE-mode leakage.

Figure S19. EL polarization characteristics of the type-B LP-QLED at various emission angles.

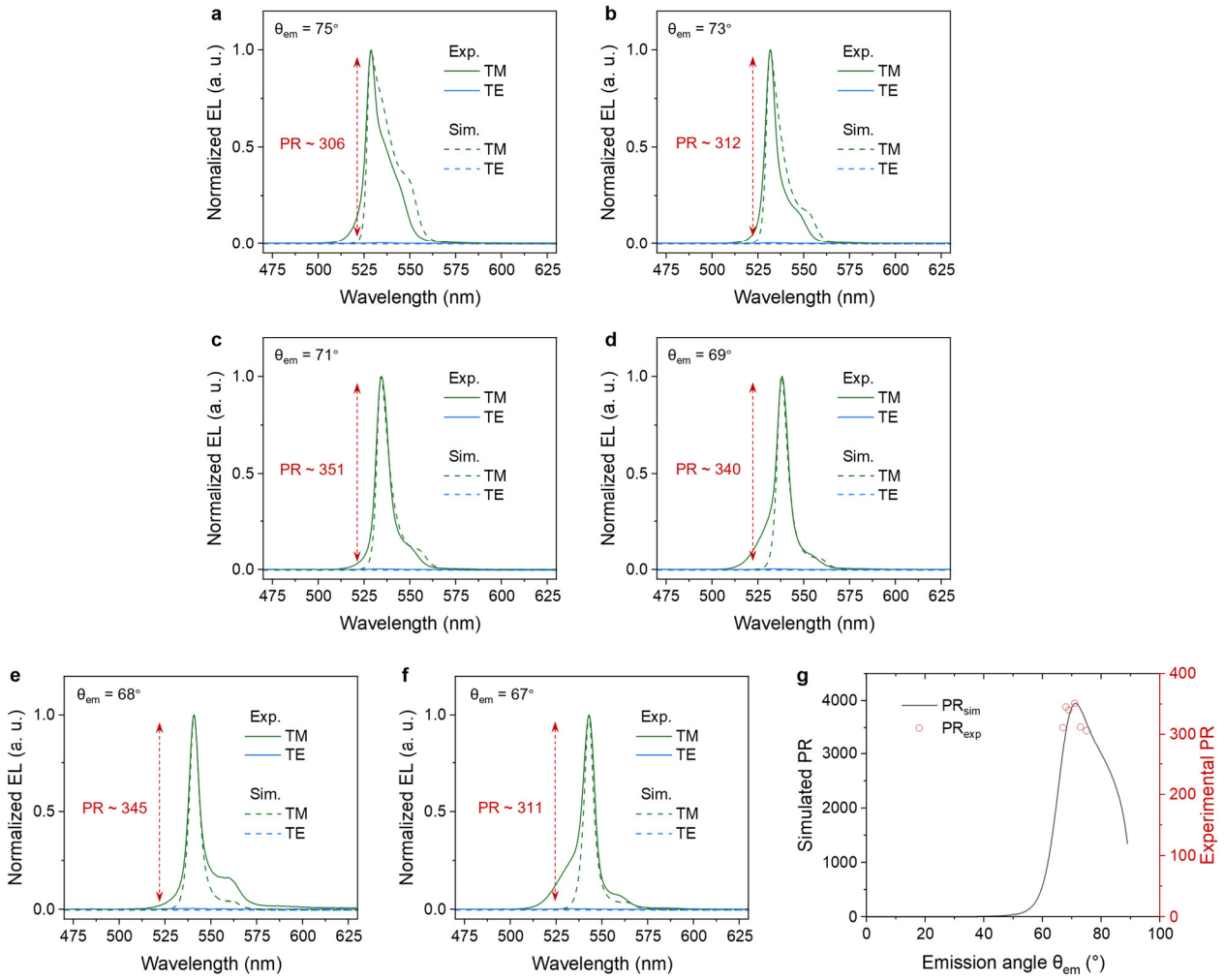

(a-f) Experimental (solid lines) and simulated (dashed lines) EL spectra of type-B LP-QLED for both TM and TE modes, measured at emission angles θ_{em} of (a) 75°, (b) 73°, (c) 71°, (d) 69°, (e) 68° and (f) 67°. The corresponding experimental PR is indicated in each panel.

(g) θ_{em}-dependent simulated (solid line) and experimental (open circles) PR values, showing a peak near θ_{em} = 71°.

Figure S20. Emission polarization characteristics of a commercial 532 nm diode-pumped solid-state (DPSS) laser.

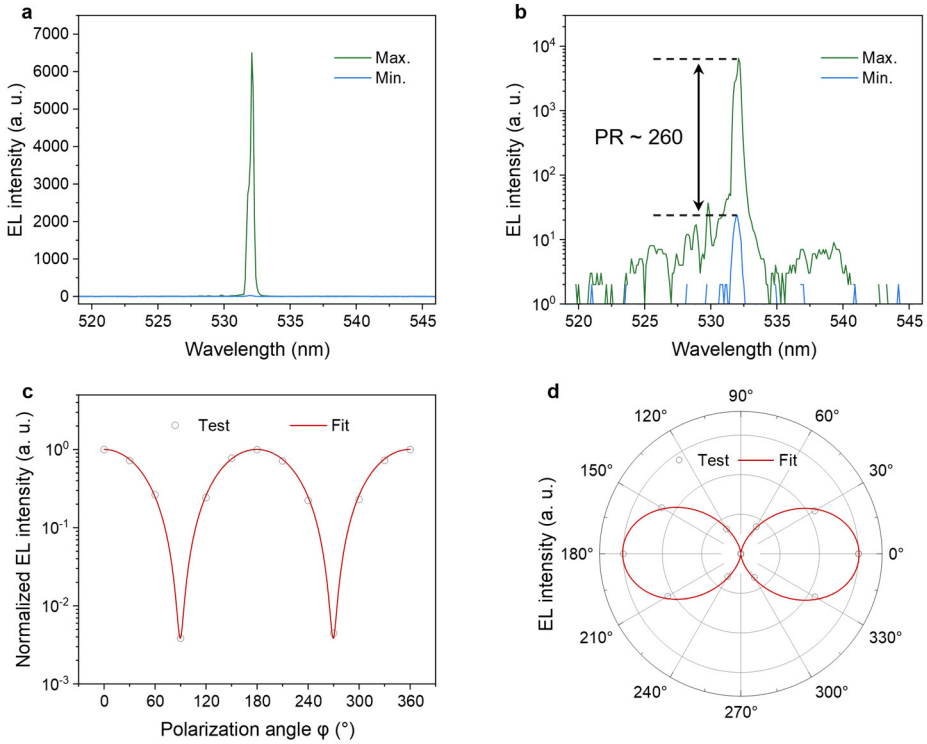

(a, b) Measured emission spectra for two orthogonal linear polarization states, plotted on a linear scale (a) and a logarithmic scale (b). The logarithmic plot reveals the high extinction between the maximum and minimum intensity signals, yielding a PR of approximately 260.

(c, d) Polarization-dependent EL intensity as a function of the polarizer angle φ. Open circles represent the experimental data, while the solid red lines are fits, confirming the strong linear polarization of the DPSS laser emission.

Table S1. Performance benchmark of reported LP EL devices categorized by emitter type.

Emitter		λ_{peak}, FWHM (nm)	Experimental PR	Experimental DOP (%)	Reference
Inorganics	InGaN/GaN quantum wells	550, 80	7	75	Appl. Phys. Lett. 95, 261110 (2009)
		513, 46	49	96	Appl. Phys. Lett. 98, 011110 (2011)
		465, /	16.7	88.7	Light Sci. Appl. 1, e22 (2012)
		500-515, 47	4.13	61	Sci. Rep. 6, 28312 (2016)
		533, 45	316	99.4	Nanoscale 9, 9104–9111 (2017)
		530, /	5.67	70	Appl. Phys. Lett. 117, 181105 (2020)
		440, /	26	92.6	Appl. Phys. Lett. 122, 111107 (2023)
		455, 32	224	99.1	Nano Letters 25, 236-243 (2025)
	Two-dimensional ReS_2	790-808, /	~9	~80	Adv. Mater. 32, 2001890 (2020)
	AlInP/AlGaInP quantum wires	580-650, /	1.86	~30	ACS Photonics 5, 1318−1325 (2018)
	InGaN/GaN quantum wells + phosphor	White	~141	~98.6	Appl. Phys. Express 10, 012101 (2017)
Organics	AC5	515, 42	70	97.2	Appl. Phys. Lett. 97, 173301 (2010)
	F8BT	540, 77	62.5	96.9	Adv. Mater. 29, 1702598 (2017)
	F8BT	564, 6	1.1	4.8	Nat. Commun. 10, 1614 (2019)
	Mixture	560, ~150	60.8	96.8	Laser Photonics Rev. 14, 1900341 (2020)
	$Ir(ppy)_3$	520, 20	13	85.7	Adv. Mater. 33, 2006801 (2021)
	BP1T-CN	493, 15	176	98.9	Optica 9, 121-129 (2022)
	$Ir(ppy)_2(acac)$	520, /	>30	>93.5	ACS Photonics 10, 3342−3349 (2023)
	DPA	470, 36	6.69	74.0	Adv. Mater. 35, 2208789 (2023)
	F8BT	540, 81	395	99.5	Adv. Optical Mater. 12, 2302950 (2024)
	FIrPic	470, 28	38	94.9	Nat. Commun. 15, 1331 (2024)
	$Ir(MDQ)_2$	609, ~67	4.88	66	Laser Photonics Rev. 2400393 (2024)
	DBTVB	460, ~90	39	95.0	Mater. Horiz. 12, 2587-2591 (2025)
	TTPSB	627, 4.1	170	98.8	Light. Sci. Appl. 13, 191 (2024)
	DPA	450, /	~19	~90	Nat. Photon. 19, 378-386 (2025)
Perovskites	$CsPbBr_3$ nanowires	519, 25	~1.62	~23.7	Chem. Commun. 56, 5413 (2020)
	$CsPbBr_3$:AD1	520, 21	2.77	47	Adv. Optical Mater. 8, 1901824 (2020)
	$PEA_2Cs_{n-1}Pb_nBr_{3n+1}$ thin film	512, ~21	2.23	38	ACS Nano 18, 29261−29272 (2024)
	$MAPbI_3$	773, ~35	3.11	51.3	Nanoscale 17, 4732-4739 (2025)
	$CsPbI_3$ nanoplatelets	620, 59	6.81	74.4	Nat. Photon. 18, 586–594 (2024)
Colloidal nanocrystals	CdSe/CdS quantum rods	620, 42	1.6	23.1	Adv. Mater. 17, 1436-1439 (2005)
		613, 33	~1.56	~21.9	ACS Nano 3, 6, 1506–1512 (2009)
		628, 41	1.25	11.1	Small 17, 2101204 (2021)
		628, /	2	33.3	Applied Surface Science 614, 156160 (2023)
	Strain-graded CdSe/ZnSe quantum dots	590, 14	~5.25 (green)	~68 (green)	Nat. Commun. 15, 5561 (2024)
	$CdSe/Cd_{1-x}Zn_xSe/ZnSe_{0.5}S_{0.5}/ZnS$ quantum dots	~626, ~30 (multi-band)	~2.5	~43	Nature 617, 79–85 (2023)
	$CdZnSe/ZnSe/Zn_xCd_{1-x}S$ quantum dots	**525-545, ~8**	**351**	**99.4**	**This work**

The PR and degree of polarization (DOP) are calculated using the maximum (I_{max}) and minimum (I_{min}) intensities measured through a rotating linear polarizer, according to the formulas:

$$\mathrm{PR} = I_{\max} / I_{\min} \quad \text{and} \quad \mathrm{DOP} = (I_{\max} + I_{\min}) / (I_{\max} - I_{\min})$$

The experimental PR of ~351 achieved in this work represents a new benchmark for solution-processed devices based on perovskite and Cd-based colloidal nanocrystals, surpassing the previous record of 6.8[4] by over 50 times. The full citations for the references[1-4,12,13,17-46] listed can be found in the final reference page.

References

1 Rizzo, A. *et al.* Polarized Light Emitting Diode by Long-Range Nanorod Self-Assembling on a Water Surface. *ACS Nano* **3**, 1506-1512 (2009). https://doi.org:10.1021/nn900063m

2 Hikmet, R. A. M., Chin, P. T. K., Talapin, D. V. & Weller, H. Polarized-Light-Emitting Quantum-Rod Diodes. *Advanced Materials* **17**, 1436-1439 (2005). https://doi.org:https://doi.org/10.1002/adma.200401763

3 Wei, Y. *et al.* CsPbBr3 nanowire polarized light-emitting diodes through mechanical rubbing. *Chemical Communications* **56**, 5413-5416 (2020). https://doi.org:10.1039/c9cc10033d

4 Ye, J. *et al.* Direct linearly polarized electroluminescence from perovskite nanoplatelet superlattices. *Nature Photonics* **18**, 586-594 (2024). https://doi.org:10.1038/s41566-024-01398-y

5 Xu, H. *et al.* Dipole–dipole-interaction-assisted self-assembly of quantum dots for highly efficient light-emitting diodes. *Nature Photonics* **18**, 186-191 (2024). https://doi.org:10.1038/s41566-023-01344-4

6 Zeng, Y. *et al.* 22% Record Efficiency in Nanorod Light-Emitting Diodes Achieved by Gradient Shells. *Advanced Materials* **36**, 2310705 (2024). https://doi.org:https://doi.org/10.1002/adma.202310705

7 Cui, J. *et al.* Efficient light-emitting diodes based on oriented perovskite nanoplatelets. *Science Advances* **7**, eabg8458 (2021). https://doi.org:doi:10.1126/sciadv.abg8458

8 Zeng, Y. *et al.* High-Efficiency and Stable Colloidal One-Dimensional Core/Shell Nanorod Light-Emitting Diodes. *Nano Letters* **24**, 5647-5655 (2024). https://doi.org:10.1021/acs.nanolett.4c01166

9 Zhu, Y. *et al.* Highly Efficient Light-Emitting Diodes Based on Self-Assembled Colloidal Quantum Wells. *Advanced Materials* **35**, 2305382 (2023). https://doi.org:https://doi.org/10.1002/adma.202305382

10 Gao, Y., Weidman, M. C. & Tisdale, W. A. CdSe Nanoplatelet Films with Controlled Orientation of their Transition Dipole Moment. *Nano Letters* **17**, 3837-3843 (2017). https://doi.org:10.1021/acs.nanolett.7b01237

11 Scott, R. *et al.* Directed emission of CdSe nanoplatelets originating from strongly anisotropic 2D electronic structure. *Nature Nanotechnology* **12**, 1155-1160 (2017). https://doi.org:10.1038/nnano.2017.177

12 Wang, M. *et al.* Metasurface integrated high energy efficient and high linearly polarized InGaN/GaN light emitting diode. *Nanoscale* **9**, 9104-9111 (2017). https://doi.org:10.1039/c7nr00539c

13 Choi, G. J. *et al.* Ultrahigh Polarization of Emitted Light by Quenched Emissive Material. *Advanced Optical Materials* **12** (2024). https://doi.org:10.1002/adom.202302950

14 Gierl, C., Zogal, K., Paul, S. & Küppers, F. *Tunable MEMS-VCSEL with >140-nm tuning range using tuning range using SiO2/SiC-based MEMS-DBR*. Vol. 9001 (SPIE, 2014).

15 Wang, Y., Pu, C., Lei, H., Qin, H. & Peng, X. CdSe@CdS Dot@Platelet Nanocrystals: Controlled Epitaxy, Monoexponential Decay of Two-Dimensional Exciton, and Nonblinking Photoluminescence of Single Nanocrystal. *Journal of the American Chemical Society* **141**, 17617-17628 (2019). https://doi.org:10.1021/jacs.9b06932

16 Mei, G. *et al.* Microcavity Design Upping Light Extraction Efficiency over 50% in High-Index Perovskite Light-Emitting Diodes. *Advanced Optical Materials* **11**, 2300912 (2023). https://doi.org:https://doi.org/10.1002/adom.202300912

17 Zhang, L., Teng, J. H., Chua, S. J. & Fitzgerald, E. A. Linearly polarized light emission from InGaN light emitting diode with subwavelength metallic nanograting. *Applied Physics Letters* **95** (2009). https://doi.org:10.1063/1.3276074

18 Brinkley, S. E. *et al.* Polarized spontaneous emission from blue-green m-plane GaN-based light emitting diodes. *Applied Physics Letters* **98** (2011). https://doi.org:10.1063/1.3541655

19 Matioli, E. *et al.* High-brightness polarized light-emitting diodes. *Light: Science & Applications* **1**, e22-e22 (2012). https://doi.org:10.1038/lsa.2012.22

20 Park, H. K. *et al.* Horizontally assembled green InGaN nanorod LEDs: scalable polarized surface emitting LEDs using electric-field assisted assembly. *Scientific Reports* **6** (2016). https://doi.org:10.1038/srep28312

21 Zhang, H. *et al.* High polarization and fast modulation speed of dual wavelengths electroluminescence from semipolar (20-21) micro light-emitting diodes with indium tin oxide surface grating. *Applied Physics Letters* **117** (2020). https://doi.org:10.1063/5.0022412

22 Huang, J. *et al.* Linearly polarized light emission from GaN micro-LEDs for 3D display. *Applied Physics Letters* **122** (2023). https://doi.org:10.1063/5.0137993

23 Wang, X. *et al.* Highly Efficient and Linearly Polarized Light Emission of Micro-LED Integrated with Double-Functional Meta-Grating. *Nano Letters* **25**, 236-243 (2025). https://doi.org:10.1021/acs.nanolett.4c04914

24 Wang, J. *et al.* Polarized Light-Emitting Diodes Based on Anisotropic Excitons in Few-Layer ReS2. *Advanced Materials* **32** (2020). https://doi.org:10.1002/adma.202001890

25 Pescaglini, A. *et al.* Three-Dimensional Self-Assembled Columnar Arrays of AlInP Quantum Wires for Polarized Micrometer-Sized Amber Light Emitting Diodes. *ACS Photonics* **5**, 1318-1325 (2018). https://doi.org:10.1021/acsphotonics.7b01257

26 Chen, L. *et al.* Highly linearly polarized white light emission from InGaN light-emitting diode with nanograting-integrated fluorescent ceramics. *Applied Physics Express* **10** (2016). https://doi.org:10.7567/apex.10.012101

27 Yomogida, Y. *et al.* Green light emission from the edges of organic single-crystal transistors. *Applied Physics Letters* **97** (2010). https://doi.org:10.1063/1.3504690

28 Choi, G. J. *et al.* Polarized Light-Emitting Diodes Based on Patterned MoS2 Nanosheet Hole Transport Layer. *Advanced Materials* **29** (2017). https://doi.org:10.1002/adma.201702598

29 Wang, M., Lin, J., Hsiao, Y. C., Liu, X. & Hu, B. Investigating underlying mechanism in spectral narrowing phenomenon induced by microcavity in organic light emitting diodes. *Nat Commun* **10**, 1614 (2019). https://doi.org:10.1038/s41467-019-09585-0

30 Zhou, L. *et al.* Tailored Polarization Conversion and Light-Energy Recycling for Highly Linearly Polarized White Organic Light-Emitting Diodes. *Laser & Photonics Reviews* **14** (2020). https://doi.org:10.1002/lpor.201900341

31 Fu, X. *et al.* Directional Polarized Light Emission from Thin-Film Light-Emitting Diodes. *Advanced Materials* **33** (2021). https://doi.org:10.1002/adma.202006801

32 An, M.-H. *et al.* Highly polarized emission from organic single-crystal light-emitting devices with a polarization ratio of 176. *Optica* **9** (2022). https://doi.org:10.1364/optica.442016

33 Dong, Q. *et al.* High-Efficiency Linearly Polarized Organic Light-Emitting Diodes. *ACS Photonics* **10**, 3342-3349 (2023). https://doi.org:10.1021/acsphotonics.3c00812

34 Jia, R. *et al.* Highly Efficient Inherent Linearly Polarized Electroluminescence from Small-Molecule Organic Single Crystals. *Advanced Materials* **35** (2023). https://doi.org:10.1002/adma.202208789

35 Chen, R., Liang, N. & Zhai, T. Dual-color emissive OLED with orthogonal polarization modes. *Nature Communications* **15** (2024). https://doi.org:10.1038/s41467-024-45311-1

36 Wang, S. R. *et al.* Polarized and Directional Electroluminescence from Organic Light-Emitting Devices by Using a Bifunctional Meta-Electrode. *Laser & Photonics Reviews* (2024). https://doi.org:10.1002/lpor.202400393

37 Pang, A. *et al.* Highly polarized single-crystal organic light-emitting devices with low turn-on voltage and high brightness. *Materials Horizons* **12**, 2587-2591 (2025). https://doi.org:10.1039/D4MH01376J

38 De, J. *et al.* Organic polaritonic light-emitting diodes with high luminance and color purity toward laser displays. *Light: Science & Applications* **13**, 191 (2024). https://doi.org:10.1038/s41377-024-01531-0

39 Qin, Z. *et al.* Intrinsically white organic polarized emissive semiconductors. *Nature Photonics* **19**, 378-386 (2025). https://doi.org:10.1038/s41566-024-01609-6

40 Zhang, J. *et al.* Strong Linearly Polarized Photoluminescence and Electroluminescence from Halide Perovskite/Azobenzene Dye Composite Film for Display Applications. *Advanced Optical Materials* **8** (2020). https://doi.org:10.1002/adom.201901824

41 Xiao, M. *et al.* Coherence Programming for Efficient Linearly Polarized Perovskite Light-Emitting Diodes. *ACS Nano* **18**, 29261-29272 (2024). https://doi.org:10.1021/acsnano.4c11761

42 Chiang, L.-M. *et al.* A linearly polarized AC-driven perovskite light emitting device with nanoscale metal contact. *Nanoscale* **17**, 4732-4739 (2025). https://doi.org:10.1039/D4NR04894F

43 Rhee, S. *et al.* Polarized Electroluminescence Emission in High-Performance Quantum Rod Light-Emitting Diodes via the Langmuir-Blodgett Technique. *Small* **17**, 2101204 (2021). https://doi.org:https://doi.org/10.1002/smll.202101204

44 Shin, D. J. *et al.* Polarized emission from unidirectionally oriented semiconductor nanorods in light-emitting devices. *Applied Surface Science* **614**, 156160 (2023). https://doi.org:https://doi.org/10.1016/j.apsusc.2022.156160

45 Jung, D. *et al.* Strain-graded quantum dots with spectrally pure, stable and polarized emission. *Nature Communications* **15** (2024). https://doi.org:10.1038/s41467-024-49791-z

46 Ahn, N. *et al.* Electrically driven amplified spontaneous emission from colloidal quantum dots. *Nature* **617**, 79-85 (2023). https://doi.org:10.1038/s41586-023-05855-6